Dynamics of long bubbles propagating through cylindrical micro-pin fin arrays

I. El Mellas [a], F. Municchi [b], M. Icardi [c], M. Magnini [a,*]

[a] *Department of Mechanical, Materials and Manufacturing Engineering, University of Nottingham, Nottingham NG7 2RD, United Kingdom*
[b] *Department of Mechanical Engineering, Colorado School of Mines, 1500 Illinois St., Golden, CO 80401, United States*
[c] *School of Mathematical Sciences, University of Nottingham, Nottingham NG7 2RD, United Kingdom*

ARTICLE INFO

ABSTRACT

The dynamics of two-phase flows confined within complex and non-straight geometries is of interest for a variety of applications such as micro-pin fin evaporators and flow in unsaturated porous media. Despite the propagation of bubbles in straight channels of circular and noncircular cross-sections has been studied extensively, very little is known about the fluid dynamics features of bubbles and liquid films deposited upon the inner walls of complex geometries. In this work, we investigate the dynamics of long gas bubbles and thin films as bubbles propagate through arrays of in-line cylindrical pins of circular shape in cross-flow, for a range of capillary and Reynolds numbers relevant to heat transfer applications and flow in porous media, different pitch of the cylinders and bubble lengths. Three-dimensional numerical simulations of the two-phase flow are performed using the open-source finite-volume library OpenFOAM v.1812, using a geometric Volume of Fluid (VOF) method to capture the interface dynamics. Systematic analyses are conducted for a range of capillary numbers $Ca = 0.04 - 1$, Reynolds numbers $Re = 1 - 1000$, streamwise pitch of the cylinders $s_x = 0.125R - 2R$, with R being the radius of the pin fins, and initial bubble length $L_b = 2.5R - 12R$. The simulations reveal that when bubbles propagate through pin fin arrays, they tend to partially coat the cylinders with a thin liquid film and to expand in the cross-stream direction within the gap left between adjacent cylinders. The liquid film deposited on the cylinders is significantly thinner than that reported for straight channels and similar geometrical constraints. As the streamwise distance between the cylinders is decreased, the flow configuration tends towards that for a straight channel, whereas larger distances cause the bubble to expand excessively in the cross-stream direction, and to eventually arrest when $s_x > 2R$. Inertial effects have a strong impact on the bubble shape and dynamics when $Re > 500$, triggering time-dependent patterns that lead to bubble fragmentation and much thicker liquid films.

1. Introduction

The dynamics of gas bubbles and thin liquid films confined in narrow geometries is key to a wide variety of processes and applications encompassing flow in unsaturated porous media (Lake, 1989), two-phase heat exchangers (Magnini and Matar, 2020b), micro-chemical reactors (Thulasidas et al., 1995), biological flows (Zamankhan et al., 2018), and water transport in gas diffusion layers of PEM fuel cells (Safi et al., 2017), to name a few. The competition of viscous and surface tension forces gives origin to thin liquid films that remain trapped between the bubble surface and the walls of the confining medium (Bretherton, 1961). The thickness and topography of this liquid film is dependent on the flow conditions and the fluid properties, but is also strongly impacted by the shape of the gap through which the bubble is advancing (Wong et al., 1995). Nonetheless, the thickness and

topography of this liquid film has an important impact on the wall–fluid exchanges, because cross-stream diffusion typically dominates over other transport phenomena across the liquid film, and thus the resistance to heat and mass transport offered by the liquid film is inversely proportional to its thickness (Picchi and Poesio, 2022). For example, the heat transfer coefficient in the correspondence of an evaporating film is often estimated as λ/h, with λ being the thermal conductivity of the liquid and h the local film thickness (Thome et al., 2004; Magnini and Thome, 2017). Gas injection is the most common approach in enhanced oil recovery and the efficiency of this process increases upon reduction of the films of oil left trapped within porous rocks (Lake, 1989).

The dynamics of long bubbles and thin liquid films in confined geometries is a traditional problem in fluid mechanics and have been

---

* Corresponding author.
  E-mail address: mirco.magnini@nottingham.ac.uk (M. Magnini).

studied extensively in the configuration where straight channels are employed. Within circular channels, the work of Bretherton (1961), Taylor (1960), Aussillous and Quéré (2000) and Han and Shikazono (2009b) has led over the years to an established correlation in the form of $h/R \sim \mathrm{Ca}^{2/3}/(1+\mathrm{Ca}^{2/3}-\mathrm{We})$ that predicts the thickness of the annular and axisymmetric liquid film surrounding the bubble under a wide range of conditions within 15% accuracy. Here, Ca denotes the capillary number of the flow, $\mathrm{Ca} = \mu U/\sigma$, with μ being the liquid dynamic viscosity, U the liquid or bubble speed and σ the surface tension, and We is the Weber number, $\mathrm{We} = \rho U^2 D/\sigma$, with ρ being the liquid density and D the tube diameter. The more recent work of Magnini et al. (2017b) showed that it is actually possible to predict the entire profile of the elongated bubble, from the bubble front to the rear meniscus, and the thickness of the liquid film, simply solving a one-dimensional ordinary differential equation for the film thickness derived from lubrication theory, without any empirical coefficient. Within square and rectangular channels, the asymptotic theory of Wong et al. (1995), the experimental work of Kreutzer et al. (2005a), Han and Shikazono (2009a), and de Lózar et al. (2007), and the computational studies of Hazel and Heil (2002), de Lózar et al. (2008), Magnini and Matar (2020b) and Magnini et al. (2022), have shown that the liquid film in noncircular channels is unevenly distributed around the channel cross-section and it can be one order of magnitude smaller than that in circular channels under the same conditions. Both empirical correlations (Kreutzer et al., 2005a; Han and Shikazono, 2009a) and asymptotic laws (Wong et al., 1995; de Lózar et al., 2008; Magnini et al., 2022) are available to predict geometrical features of this liquid film in square and rectangular channels.

Conversely, the dynamics of bubbles propagating through complex and non-straight channels have received far less attention from the fundamental perspective of measurement and topography of the lubricating film. Muradoglu and Stone (2007) have studied the motion of long bubbles in curved channels using theory and numerical simulations and suggested modifications to Bretherton's law to estimate the inner and outer thickness of the lubricating film. Other works that focused on the flow of bubbles and droplets in sinusoidal and corrugated channels exist (Sauzade and Cubaud, 2018; Patel et al., 2019; Anjos, 2021), but were either limited to bubbles smaller than the channel size or did neither report systematic data for film thickness nor comparisons of film thicknesses with traditional circular or noncircular channel data. A geometric configuration often arising in practical applications of two-phase flows is flow past arrays of cylindrical obstacles in cross-flow. For example, Ferrari and Lunati (2013) have studied two-phase flow in porous media by modelling the pore geometries from a two-dimensional packing of circles. In the absence of established methods to predict liquid film thickness through such complex geometries, flat-plate models and Bretherton's law for circular channels are still utilised to model the two-phase dynamics (Gomes Suarez et al., 1999; Shang et al., 2008). Micro-pin fin heat exchangers have recently emerged as an alternative to multi-microchannels evaporators for two-phase cooling of high power-density electronics, as they enhance mixing and promote uniform flow distribution across the flow region (Renfer et al., 2013). For example, Falsetti et al. (2017a,b, 2018a) characterised the heat transfer performance of a micro-evaporator of base area 1×1 cm^2 where 66 rows of in-line circular pin fins of diameter of 50 μm and height 100 μm were arranged in cross-flow. Vapour bubbles were observed to nucleate over the surface of the pin fins and grow along the gaps in between the pin fins arrays. Many other studies are available in the literature concerning boiling heat transfer in miniaturised pin fin evaporators, with pin fin cross-sectional geometries varying from circular (Kosar and Peles, 2006; Krishnamurthy and Peles, 2010) to square, diamond (Wan et al., 2017), and hydrofoil-based (Kosar and Peles, 2007). However, the aforementioned studies were focused on the heat transfer performance and no liquid film thickness dynamics or measurements were reported. Falsetti et al. (2018b) proposed a phenomenological boiling heat transfer model for micro-pin fin evaporators

based on Thome et al. (2004) three-zone model for slug flow, and estimated the thickness of the lubricating film over the channels base and top surfaces and pin fin surfaces using Han and Shikazono (2009b) correlation for circular channels, adjusted to capture the complex evaporator geometry. The correctness of this approach could not be verified as no direct measurement of the film thickness was performed in the experiment.

In summary, the overview of the literature outlined above emphasises that while there exist extensive datasets and established correlations to predict the dynamics of long bubbles and thin liquid films in straight channels, there is a lack of data and modelling tools for bubble and film dynamics in more complex geometries, which are relevant to a number of applications such as flow in porous media and pin fin heat exchangers.

To fill this gap, we have performed a fundamental study of long gas bubbles transported by a liquid flow between arrays of cylindrical pin fins, in adiabatic conditions. The study is done by means of numerical simulations, using a Volume-Of-Fluid (VOF) method as implemented in the TwoPhaseFlow library for OpenFOAM v1812 released by Scheufler and Roenby (2021). We employ a three-dimensional representation of the geometry and flow, where the long gas bubble translates between two arrays of circular pin fins, and we report the topography and thickness of the liquid film left over the cylindrical obstacles upon the passage of the bubbles, by systematically varying both the capillary and Reynolds number of the flow in conditions relevant to flow in porous media and two-phase cooling. Additionally, we study the impact of the distance between the obstacles and bubble length on the two-phase flow dynamics. The rest of this article is organised as follows: the numerical framework is described in Section 2; Section 3 outlines the results of validation tests; the model geometry and the results of the mesh convergence analysis are reported in Section 4; Section 5 provides the results of the systematic study conducted to cover a wide range of flow and geometrical parameters; the conclusions are summarised in Section 6.

2. Numerical framework

Direct numerical simulations of unsteady, isothermal and laminar flow are performed using the open-source library OpenFOAM. OpenFOAM is a finite-volume framework developed in C++ with a focus on Computational Fluid Dynamics. The fluid model solves the Navier–Stokes equations for the flow of two immiscible phases, specifically gas and liquid, separated by an interface. Both phases are treated as incompressible, Newtonian fluids. A single-fluid formulation is adopted, and the two phases are treated as a single mixture of fluid with variable properties over the interface, such that a single field of velocity and pressure are sufficient to describe the flow. Therefore, a single set of conservation equations is used all over the domain (Tryggvason et al., 2011).

2.1. Governing equations

The two-phase flow is resolved by using OpenFOAM's geometric VOF solver isoAdvector (Roenby et al., 2016) in conjunction with the libraries to improve interface advection (Scheufler and Roenby, 2019) and surface tension reconstruction with the recently released TwoPhaseFlow library by Scheufler and Roenby (2021), which was compiled on ESI-OpenFOAM v.1812. A single set of the governing equations for mass and momentum is formulated and solved over the entire computational domain, these can be expressed as follows:

$$\nabla \cdot \boldsymbol{u} = 0 \tag{1}$$

$$\frac{\partial(\rho\boldsymbol{u})}{\partial t} + \nabla \cdot (\rho\boldsymbol{u}\boldsymbol{u}) = -\nabla p + \nabla \cdot \mu\left[(\nabla\boldsymbol{u}) + (\nabla\boldsymbol{u})^T\right] + \boldsymbol{F_\sigma} \tag{2}$$

where $\boldsymbol{u}$ indicates the fluid velocity, ρ the mixture fluid density, t the time, p the pressure, μ the dynamic viscosity, and $\boldsymbol{F_\sigma}$ the surface

tension force vector. Details of the surface tension model are provided in the next subsection. Gravitational effects are neglected in this work. In order to describe and localise the interface between the two fluids, an additional transport equation is solved. The VOF method is adopted as the interface capturing method; a volume fraction field α is defined to identify the different phases throughout the flow domain. In each computational cell of the domain, α identifies the fraction of the computational cell volume occupied by the primary phase, which coincides with liquid in the present study. Therefore, the volume fraction takes values of 1 in the liquid, 0 in the gas, and $0 \leq \alpha \leq 1$ in the interfacial cells, where the liquid–gas interface can be found. Accordingly, an additional transport equation for the volume fraction is solved:

$$\frac{\partial \alpha}{\partial t} + \nabla \cdot (\alpha \boldsymbol{u}) = 0 \qquad (3)$$

Using the volume fraction field, the properties of the mixture fluid can be computed as an average over the two phases, e.g. $\rho = \alpha \rho_l + (1-\alpha)\rho_b$, with the subscripts b and l denoting gas- (bubble) and liquid-specific properties, respectively. All the fluid-specific properties (e.g. ρ_b, ρ_l, μ_b, μ_l, etc.) are considered constant in this work.

2.2. Surface tension model

The surface tension force, $\boldsymbol{F}_\sigma$ in Eq. (2), is formulated according to the Continuum Surface Force method (Brackbill et al., 1992) and computed as:

$$\boldsymbol{F}_\sigma = \sigma \kappa \nabla \alpha \qquad (4)$$

where σ is the surface tension coefficient (considered constant) and κ is the local interface curvature. The native VOF solvers of OpenFOAM evaluate κ as the gradient of the volume fraction, $\kappa = \nabla \cdot (\nabla\alpha/|\nabla\alpha|)$. The accuracy of the computation of κ has a significant influence in this type of simulation (Abadie et al., 2015), where the surface tension dominates the dynamics of the flow. Numerical errors lead to the generation of spurious velocity fields, whose intensity is higher as the flow is slower because the spurious currents' magnitude is inversely proportional to the capillary number. The TwoPhaseFlow library allows different choices to calculate κ based on various approximations of the interface. For the work presented in this study, a Reconstructed Distance Function (RDF) model was selected. The RDF algorithm is based on an implementation of the model proposed by Cummins et al. (2005). The RDF model shares many similarities with coupled Level Set and Volume of Fluid (CLSVOF) models, the main difference being that, in the RDF, the signed distance function ψ is not found solving a transport equation as in LS methods, but it is constructed geometrically based on the α field (Scheufler and Roenby, 2021). The algorithm, in the first step, calculates the ψ in the cell centre of a narrow band of cells around the interface:

$$\psi_{cc} = \boldsymbol{n}_s \cdot (\boldsymbol{x}_{cc} - \boldsymbol{x}_s) \qquad (5)$$

where ψ_{cc} denotes the distance from the cell centre ($\boldsymbol{x}_{cc}$) to an interface segment ($\boldsymbol{x}_s$). The interface normal $\boldsymbol{n}_s$ is approximated with a least-squares fit as $\boldsymbol{n}_s = \nabla\psi$. The gradient of the signed function is then evaluated as $\boldsymbol{n}_\psi = \nabla\psi/|\nabla\psi|$. After that, the curvature is computed by interpolating $\boldsymbol{n}_\psi$ from the cell centres to cell faces and applying the Gauss–Green gradient method:

$$\kappa = \nabla \cdot \boldsymbol{n}_\psi \rightarrow \kappa_{cc} \approx \frac{1}{V_{cc}} \sum_f \boldsymbol{n}_{\psi,f} \cdot \boldsymbol{S}_f \qquad (6)$$

where the V_{cc} is the cell volume and $\boldsymbol{S}_f$ is the face area vector pointing out of the cell. The drawback of this method appears in the case of unstructured grids where inaccuracies may arise due to interpolation errors. These can be reduced by computing κ with the use of a least-squares gradient method. Further details about the algorithm are provided by Scheufler and Roenby (2021). A comparison of the different surface tension modules available in the library TwoPhase-Flow with OpenFOAM's interFoam and isoAdvector built-in methods has been provided by Magnini et al. (2022).

2.3. Discretisation methods

The governing equations are solved using OpenFOAM, version v.1812, with the VOF library TwoPhaseFlow developed by Scheufler and Roenby (2021). The transport equations are discretised with a finite-volume method on a collocated grid arrangement. The library is composed of two main classes: one for the interface reconstruction scheme and one for the volume fraction advection scheme. The advection scheme base class allows integration of other advection schemes such as level-set or phase field methods. This way, the user can select whether to run the solver using the algebraic VOF (interFoam mode) or to use the geometric VOF (isoAdvector mode) with any of the built-in interface reconstruction methods (isoAlpha, isoRDF, plicRDF; see Scheufler and Roenby (2019)). Among the different VOF solvers in OpenFOAM, we adopted the geometric method isoAdvector, with the advection method set on *isoAlpha, nAlphaSubCycles 1* and *nAlphaBounds 3*. The isoAdvector solver is preferred over the algebraic VOF due to excellent results in terms of volume conservation, interface sharpness, boundedness, and shape preservation. The method also yields a more accurate interface characterisation in complex flow dynamics and arbitrary meshes, enabling larger time steps.

All other equations are integrated in time with a second-order implicit Crank–Nicolson scheme with a blending coefficient of 0.9 to ensure accuracy and robustness. The divergence operators are discretised using second-order TVD (Total Variation Diminishing) schemes (van Leer, 1979), whereas Laplacian operators are discretised with central finite-differences. The PIMPLE algorithm, a combination of PISO (Pressure Implicit with Splitting of Operator) and SIMPLE (Semi-Implicit Method for Pressure-Linked Equations) (Issa, 1985) is utilised to iteratively update pressures and velocities (*momentumPredictor no*; *nCorrectors 3*) within each time step. The residuals thresholds for the iterative solution of the flow equations are set to 10^{-7} for the velocity, 10^{-8} for the pressure, and 10^{-8} for the volume fraction. The time-step of the simulation is variable and is calculated based on a maximum allowed Courant number of 0.05, unless otherwise specified.

3. Validation

The present numerical framework was validated by Magnini et al. (2022) with the simulation of long gas bubbles propagating in straight rectangular channels of different aspect-ratio, and comparison against benchmark liquid film thickness data from the literature. No literature data is available for the isothermal flow of long bubbles between pin fin arrays, and thus we have performed new validation tests by considering a confined, elongated gas bubble travelling steadily into straight 2D and circular (axisymmetric) channels. Even though the flow configuration differs from flow past cylindrical obstacles, we expect that the validation of the numerical framework over a broad range of geometrical configurations is sufficient to verify the accuracy of the numerical model. Furthermore, the dynamics of long bubbles in 2D configurations (flow between parallel plates or within circular pipes) is well established and will serve as a comparison for the simulations of flow past pin fins presented in the next sections.

The flow configuration analysed in this section is exemplified in Fig. 1(a), which provides a snapshot of a long bubble passing through a 2D straight channel, at steady-state. We consider the benchmark Bretherton problem (Bretherton, 1961), where a long gas bubble propagates in a straight channel under the effect of a net liquid inflow. Owing to the competition of viscous and capillary forces, the bubble traps a thin liquid film against the wall. The main parameter describing the profile and thickness of this film is the capillary number, which compares viscous and capillary effects, $Ca = \mu_l U/\sigma$, with U being either the bubble U_b or the cross-sectional average liquid velocity U_l. Inertial forces may have a role on the bubble dynamics (Han and Shikazono, 2009a), and these are described by the Reynolds number
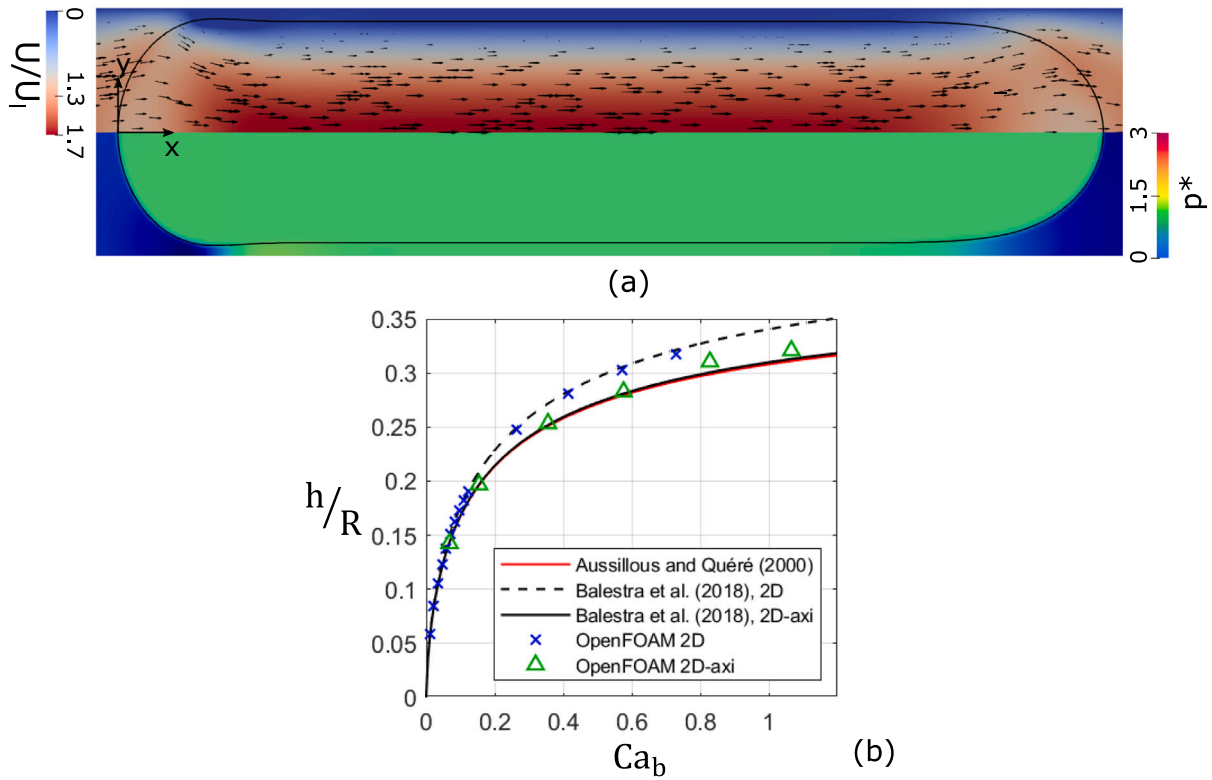
Fig. 1. Results for the validation case of a long bubble translating in a 2D and 2D axisymmetric channel. (a) Snapshot of a confined elongated bubble passing through a 2D straight channel, considering the results for capillary number $Ca_l = 0.03$. In the image, pressure (bottom half) and velocity fields (top half) are displayed. The velocity field is rescaled by the average liquid speed (U_l); the pressure field is rescaled by the capillary pressure $p_{ref} = \sigma/R$. (b) Dimensionless liquid film thickness (h/R) against bubble capillary number. As a reference, the graph includes also the film thickness predictions obtained using the correlations of Aussillous and Quéré (2000) for circular channels, and of Balestra et al. (2018) for both 2D planar and 2D axisymmetric cases.

$Re = 2\rho_l U R/\mu_l$, with R being the channel radius (pipe flow) or semi-height (2D flow). Gravitational effects are neglected in this study, as we are interested in microfluidic conditions where the Bond number is much smaller than unity.

In the numerical model, we consider both two-dimensional and axisymmetric ducts of semi-height (or radius) R and length $40R$, which is sufficient for the bubble to reach steady conditions. At the inlet, a fully-developed laminar profile is imposed to the fluid velocity, together with a null pressure gradient. No-slip is applied to the walls. At the outlet, a constant pressure is imposed, together with a null velocity gradient. As initial conditions, a long gas bubble with circular ends is set near the channel inlet; the bubble is long enough such that a flat film region establishes between the front and rear menisci. The liquid-to-gas density and viscosity ratios are set to $\rho_l/\rho_g = 1000$ and $\mu_l/\mu_g = 100$, to represent typical air–water cases or refrigerants used in two-phase cooling applications (Falsetti et al., 2018a).

For this validation study, we have tested a wide range of liquid capillary numbers $Ca_l = \mu_l U_l/\sigma = 0.01$–$0.5$, which resulted into a range of bubble capillary numbers $Ca_b = \mu_l U_b/\sigma = 0.0105$–$1$, to cover the range investigated in the next sections for flow past pin fins. The Reynolds number of the flow is set to a small reference number, $Re_l = 1$, for which inertial effects are expected to be small (Magnini et al., 2017b). This enables comparison of results with literature data for the visco-capillary regime (Aussillous and Quéré, 2000).

To achieve correct liquid film thickness values in the simulation, the computational mesh must be sufficiently fine to fully discretise the flow in the thin liquid film, with the smallest capillary number tested posing the most severe conditions. Using Aussillous and Quéré (2000) correlation, we estimate a film thickness of about $h/R \approx 0.05$ for $Ca_l = 0.01$. Accordingly, we use a structured orthogonal mesh with 60 square cells in the radial direction, which are gradually refined in

a boundary layer of thickness $0.05R$ near the wall, made of 14 cells with minimum thickness of about $0.001R$. This guarantees that there are always more than 10 cells discretising the film region, in agreement with a previous study under similar conditions (Khodaparast et al., 2015). Overall, the computational domain includes nearly 200,000 cells and all the simulations were performed using a workstation. With 16 cores, the computational time required for each simulation to achieve steady-state was of about 16 CPU hours.

Fig. 1(a) illustrates a snapshot of bubble profile, velocity and pressure contours, at steady-state for $Ca_l = 0.03$ and a two-dimensional non-axisymmetric configuration. It can be seen that a thin liquid film is present next to the wall, where the flow is stagnant. This is expected, because there is no curvature gradient in the bubble profile that can drive flow by capillarity. Pressure is uniform within the bubble and it is interesting to note that, while a pressure jump exists across the interface at the bubble nose and rear, no pressure change occurs across the interface in the film region. This can be explained by the fact that, in the two-dimensional geometry, there is only one interface curvature (in the x–y plane), and thus where the film is flat the total curvature is zero and no Laplace pressure jump occurs. The situation differs in the axisymmetric case, because even though the interface profile appears flat along the film in the x–y plane, there is a second curvature of the bubble in the cross-stream plane which establishes a nonzero pressure jump between gas and liquid in the film region.

The liquid film thicknesses measured in the simulations for both 2D and 2D axisymmetric cases are reported in Fig. 1(b) as a function of the bubble capillary number. The graph includes also film thickness predictions obtained using the correlation of Aussillous and Quéré (2000) for circular channels, $h/R = 1.34Ca^{2/3}/(1 + 3.35Ca^{2/3})$, and the correlations developed by Balestra et al. (2018) for both planar and axisymmetric cases. Our numerical model is always very close to the

reference data, with the largest deviation of about 5% as $Ca_b \rightarrow 1$ in the circular channel case. This can be ascribed to the appearance of inertial effects in the bubble dynamics as the Weber number approaches unity (Magnini et al., 2017b), and to uncertainty in the Aussillous and Quéré (2000) correlation in this range of values; for example, if the film thickness correlation of Han and Shikazono (2009a) is utilised, the deviation with the simulation results in this range falls below 5%.

4. Model setup and mesh convergence analysis

This section introduces the model geometry and mesh for the study of the flow of long bubbles translating between pin fin arrays. We consider the flow of an isolated long gas bubble that travels through the channel formed by two arrays of in-line cylindrical pin fins of circular cross-section in cross-flow, under the effect of a liquid flow parallel to the arrays; Fig. 2 provides a schematic representation of the geometry and flow configuration. In the numerical model, the flow domain is represented with a three-dimensional geometry, as illustrated in Fig. 2(a). To describe the flow, a Cartesian reference frame is adopted, where x expresses the streamwise coordinate, y is the width-wise cross-stream coordinate and z is the height-wise cross-stream coordinate, parallel to the cylinders axes. The reference frame is centred half-way along the domain height and width, so that $z = 0$ identifies the domain's horizontal centreplane and $y = 0$ a vertical centreplane. The radius of the circular pin fins R is kept constant throughout the study; for convenience, all other dimensions are rescaled with R. Fig. 2(b) provides a schematic representation of the geometry on a horizontal centreplane ($z = 0$). The flow domain has a length of $L = 60R$. The domain cross-section has a width $W = 8R$ and height $H = 2R$, so that the cylinders height and diameter coincide. Two arrays of in-line cylindrical pin fins, illustrated as full white circles in Fig. 2(b), are positioned along the x direction, symmetric with respect to the vertical centreplane $y = 0$. The cross-stream pitch of the cylinders is maintained constant in this work, $d_y = 4R$, so that the cross-stream gap between the cylinders identifies a square channel of width $s_y = d_y - 2R = 2R$. The choice of maintaining s_y fixed and equal to $2R$ enables us to reduce the number of geometrical variables. The streamwise pitch of the cylinders is indicated as d_x, with the corresponding gap being $s_x = d_x - 2R$, and this will be changed during the study, with the baseline configuration being $s_x = 0.5R$.

As boundary conditions, a liquid-only flow of uniform velocity magnitude is imposed at the domain inlet, where the streamwise coordinate origin $x = 0$ is set, together with a zero-gradient pressure condition. Due to the symmetry of the flow, only one quarter of the domain cross-section is resolved and symmetry boundary conditions are adopted at the sides of the domain margins, corresponding to planes $y = 0$ and $y = W/2$, and on the horizontal centreplane $z = 0$. On the top ($z = H/2$) domain boundary, a no-slip condition is imposed. At the outlet boundary ($x = L$), pressure is set to a zero reference value together with a zero-gradient velocity condition. On the pin fin walls, a no-slip condition is applied. Since the lubricating film trapped between bubble and cylinders is always discretised with the mesh, no contact line forms and thus the contact angle boundary condition is not necessary. As initial condition, a long gas bubble of initial length L_b is patched along the domain centre, with the shape of a cylinder (of radius $0.9R$) with spherical rounded ends; the initial length of the bubble will be varied during the study to investigate its impact on the flow dynamics, with the baseline configuration being $L_b = 12R$. Note that this flow model, i.e. long gas bubbles travelling through arrays of pin-fins, applies well to boiling in micro-pin fin evaporators where long vapour bubbles are generated upon nucleation within the superheated fluid (Falsetti et al., 2017a), but can also be a model for the dynamics of carbon dioxide bubbles propagating through porous subsurface reservoirs in geological CO_2 sequestration (Soulaine et al., 2018).

At the onset, the bubble propagates downstream and its shape and velocity evolve towards a steady-periodic configuration; the domain

length was chosen sufficiently long in order for such regime to be achieved by the propagating bubble. Fig. 2(c) and (d) show examples of the liquid film morphology identified during the bubble transit and introduce the notation that will be later used to report liquid film thickness measurements. Surface tension forces redistribute the liquid surrounding the bubble into thin films covering the cylinders and top/bottom channel walls, similarly to what observed in square channels (Magnini and Matar, 2020a), while static menisci are formed in the gap between two consecutive cylinders. Fig. 2(d) shows a close-up view of the liquid film profile on a horizontal centreplane ($z = 0$), near the cylinder coloured in red in (b), with the dark-red area identifying the bubble. For convenience, the thickness of this film is described as the radial distance between the cylinder surface and the liquid–gas interface, measured on a local reference frame centred with the cylinder. For each cylinder, different film thickness parameters will be extracted and presented in the next sections: a local film thickness $h(\theta)$, which varies in the circumferential direction with the reference $\theta = 0$ coinciding with the y-axis; a film thickness at the cylinder centre, $h(\theta = 0) = h_c$; a circumferentially minimum film thickness value h_{min}, which does not necessarily occur at $\theta = 0$.

The aim of this work is to investigate the dynamics of long gas bubbles travelling across pin fin arrays by systematically varying capillary and Reynolds numbers, streamwise pitch of cylinders and bubble length. Capillary and Reynolds numbers based on the bubble velocity are defined as $Ca_b = \mu_l U_b / \sigma$ and $Re_b = 2\rho_l U_b R / \mu_l$, where R corresponds to the pin fin radius which in the present setup coincides with the half-height and half-width of the channel left between the in-line arrays of pin fins. The corresponding groups based on the liquid speed are evaluated by considering as U_l the average liquid velocity in the channel bounded by the pin fin arrays, which is twice the average liquid speed set at the domain inlet due to the cross-section reduction induced by the cylinders. The range of conditions investigated in this study has been chosen to be relevant to two-phase flow in micro-pin fin heat exchangers (Falsetti et al., 2018a), where $Ca = 10^{-3} – 10^{-1}$ and $Re = 10–10^3$, and flow in porous media (Roland et al., 1988; Ferrari and Lunati, 2013), where the capillary number may span several orders of magnitudes ($Ca = 10^{-6}–10^{-1}$) while $Re \ll 1$. The capillary and Reynolds numbers, streamwise pitch of cylinders and bubble length will be varied independently in this study, within the following ranges: $Ca_l = 0.04–1$, $Re_l = 1–1000$, $s_x = 0.125R–2R$, and $L_b = 2.5R–12R$. Smaller values of Ca_l are disregarded due to the computational cost of resolving very thin liquid films. Liquid-to-gas density and viscosity ratios in this work are fixed to 1000 and 100, respectively, which are representative of air–water combinations or two-phase flow of refrigerants. All fluid properties and simulation conditions utilised in this study are reported in dimensional units in the Appendix.

Our interest is to fully resolve the flow in the thin liquid film trapped between the pin fins and the long bubble, and therefore the computational mesh must be sufficiently fine to discretise this film with an adequate number of cells under all conditions simulated. The domain is meshed in three successive steps, using OpenFOAM's library *snappyHexMesh*. First, the domain block without pin fins is discretised with a uniform structured mesh made of cubes of side Δ, with the parameter R/Δ indicating the number of cells per radius of the cylinders. Then, the mesh is recursively refined n times near the cylinders surface, by splitting a cube into eight equal smaller cubes for each refinement cycle. We identify as $\Delta_{min} = \Delta/2^n$ the size of the smallest cubic cells obtained after n refinements, with the number of smallest cubic cells per cylinder radius quantified as R/Δ_{min}. Finally, a thin boundary layer composed of 5 cells and overall thickness $2\Delta_{min}$ is generated over the surface of the cylinders, where cells are progressively refined radially towards the cylinders surface, from Δ_{min} on the outer edge of this layer down to an absolute minimum cell thickness of $\Delta_{min}/2^4$ on the cylinder surface. A representative image of the grid arrangement for a mesh built with $R/\Delta = 40$ and $n = 2$ is shown in Fig. 3(a).
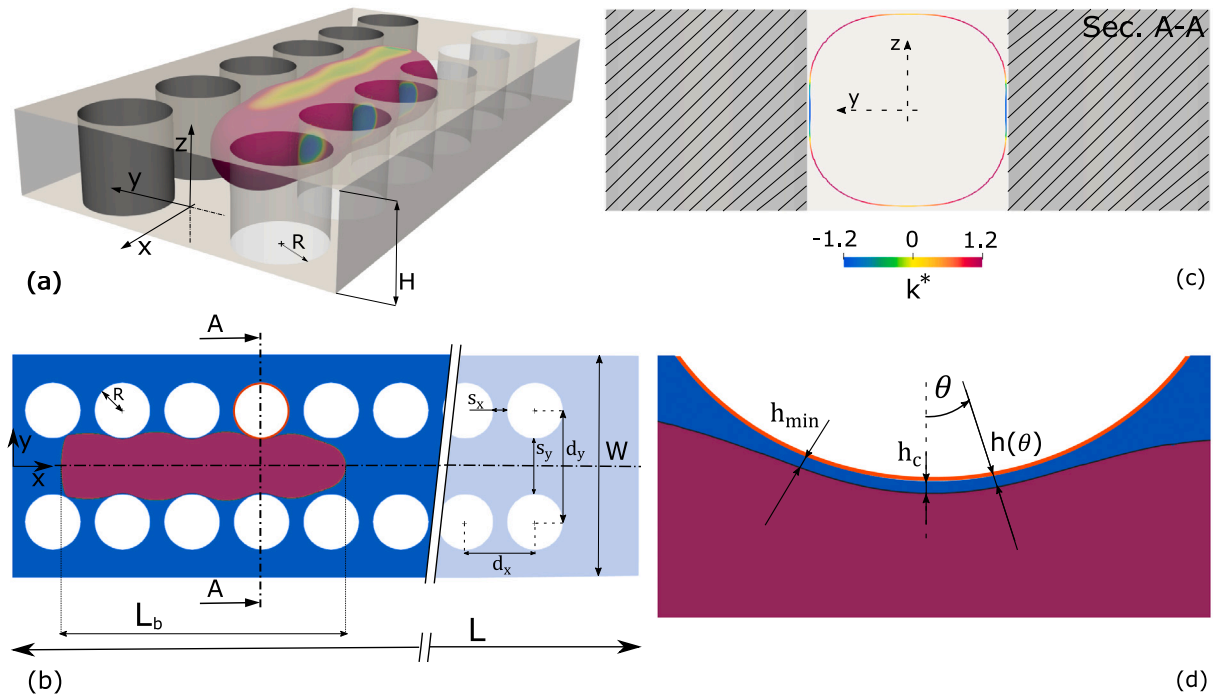
Fig. 2. (a) Illustration of the flow configuration under study. An elongated bubble propagates through the gap formed by two arrays of in-line cylindrical pins. The rainbow tinted contour identifies the bubble surface at a given time instant, coloured by the nondimensional value of the interface curvature $\kappa^* = \kappa R$. (b) Illustration of the computational domain on a horizontal centreline plane ($z = 0$). The domain width and length are indicated with W and L, respectively. R denotes the radius of the cylindrical pins. The flow is from left to right. The streamwise (along x) and cross-stream (along y) distance between the cylinders centres are indicated as d_x and d_y. The streamwise and cross-stream gap between the pins are denoted as s_x and s_y, with $s_x = d_x - 2R$ and $s_y = d_y - 2R$. The dark-red area identifies the bubble at a given time instant, and its length is denoted as L_b. (c) Cross-section of the bubble extracted on Section A–A in (b), coloured by the value of the nondimensional interface curvature. The colour legend in (c) applies also to (a). (d) Close-up view of the liquid film profile on the horizontal centreline plane ($z = 0$), near the cylinder coloured in red in (b). The liquid film thickness is measured on a local reference frame centred on the cylinder centre, and $h(\theta)$ denotes the film thickness measured along the radial direction at an angle θ from the y axis. h_c and h_{min} denote, respectively, the film thickness at $\theta = 0$ and its minimum value around the cylinder. The images above refer to a case run with $Ca_l = 0.04$, $Re_l = 1$, $s_x = 0.5R$, and initial bubble length $L_b = 12R$. (For interpretation of the references to colour in this figure legend, the reader is referred to the web version of this article.)

The mesh analysis was performed for a base case run with $Ca_l = 0.04$, $Re_l = 1$, $s_x = 0.5R$, and $L_b = 12R$. This has the smallest capillary number of the range that will be investigated, and thus represents the most severe case due to the very thin liquid film expected. Four different computational meshes were created, by fixing the background mesh size to $R/\Delta = 40$ and applying four different levels of refinement near the cylinders, $n = 0, 1, 2, 3$. Further details for these four meshes are provided in Table 1.

Fig. 3(b) displays the results of the mesh convergence analysis, presented in terms of the film thickness measured around cylinder number 12 from the domain inlet. We consider the film thickness at the cylinder centre h_c measured on a horizontal centreplane as indicated in Fig. 2(d). It will be shown in the next sections that the film thickness does never reach a constant value as the bubble is transiting, similarly to what observed in square channels by Magnini and Matar (2020a), and thus the film thickness reported in Fig. 3(b) is taken at an instant where the bubble nose is $9R$ downstream the cylinder centre. In the graph, the film thickness is plotted as a function of R/Δ_{min}, where Δ_{min} denotes the size of the smallest cubic cell in the domain.

All the meshes tested yield a film thickness value close to $h_c/R = 0.02$, and no major differences are observed in the results obtained with the different meshes. This can be explained with the fact that even the coarsest mesh ($R/\Delta = 40$, $n = 0$) discretises the film with about 4 computational cells thanks to the very thin boundary layer of cells generated around the cylinder surface, which is at the bottom limit of the threshold suggested by Gupta et al. (2009) to adequately resolve thin liquid films. Results seems to converge towards a value of h_c/R close to 0.019 as $R/\Delta_{min} > 150$, with less than 2% difference in the film thicknesses detected with the two most refined meshes (identified as mesh c and d in Table 1). Therefore, the mesh characterised by

Table 1

Details of the four computational grids tested, characterised with the number of cells per cylinder radius in the bulk flow region (R/Δ), number of recursive refinements near the cylinders walls (n), smallest size of the cubic cells in the refined region $\Delta_{min} = \Delta/2^n$ and thickness of the thinnest cell ($\Delta_{min}/2^4$) in the boundary layer surrounding the cylindrical pin fins.

Mesh convergence analysis.

Mesh	R/Δ	n	Cells number	$\Delta_{min} = \Delta/2^n$	$\Delta_{min}/2^4$
a	40	0	11 197 384	$0.025R$	$0.0016R$
b	40	1	18 966 336	$0.0125R$	$0.0008R$
c	40	2	30 341 952	$0.0062R$	$0.0004R$
d	40	3	52 916 544	$0.0031R$	$0.0002R$

$R/\Delta = 40$ and $n = 2$, displayed in Fig. 3(a) and identified as case c in Table 1, is the one selected for the remainder of this work. Simulations were run on the high-performance computing cluster Sulis at HPC Midlands+ (https://warwick.ac.uk/research/rtp/sc/sulis). Using typically 256 cores and OpenFOAM's scotch domain decomposition, the computational time for each simulation ranged from 10,000 (high Ca_l) to 50,000 CPU hours (low Ca_l).

5. Results

The results of the systematic analysis of the flow of long bubbles between arrays of in-line cylindrical pin fins are presented below, organised in subsections. Section 5.1 reports in detail the findings for a reference case run with $Ca_l = 0.04$, $Re_l = 1$, $s_x = 0.5R$ and $L_b = 12R$. Section 5.2 presents the results of the visco-capillary regime, where the Reynolds number is fixed to a very small number ($Re_l = 1$) so that inertial effects are negligible, and the liquid film thickness and
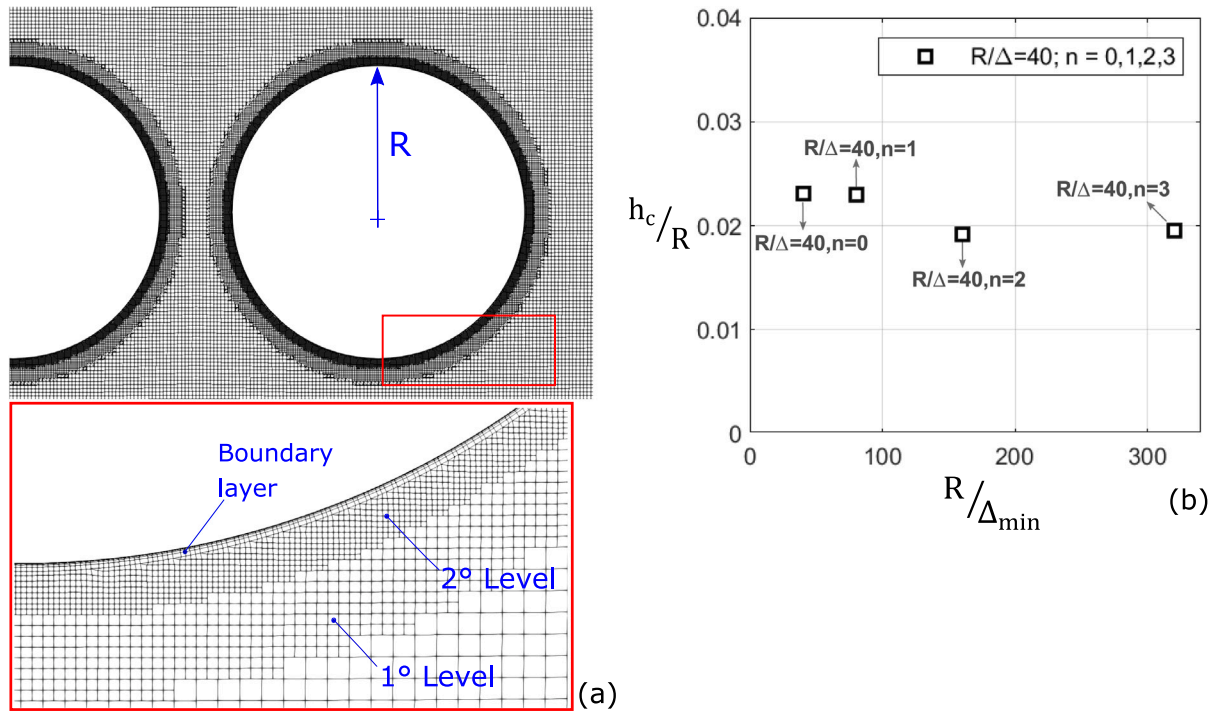
Fig. 3. Results for the mesh convergence analysis for a long bubble translating through micro-pin fin arrays. (a) Example of computational mesh and close-up view of the refined regions near a cylinder, for the grid arrangement with $R/\Delta = 40$ and $n = 2$; Δ indicates the largest size of the cubic cells far from the cylinder, while n indicates the maximum level of refinement near the pins, which identifies the size of the smallest cubic cell as $\Delta_{min} = \Delta/2^n$. (b) Dimensionless liquid film thickness h_c/R, measured in the correspondence of the 12th cylinder from the inlet, as indicated in Fig. 2(d), for increasing values of mesh resolution. Further details about the grids are provided in Table 1.

bubble dynamics are studied by systematically varying Ca_l in the range $Ca_l = 0.04$–1. Section 5.3 describes the results of the simulations performed by changing the streamwise gap between the pins s_x for three selected values of capillary number ($Ca_l = 0.04, 0.1$ and 0.2) and $Re_l = 1$. Section 5.4 investigates the results obtained by varying the initial bubble length L_b for one value of the capillary number ($Ca_l = 0.1$). The last Section 5.5 presents the results of the visco-inertial regime, where simulations were run by varying the Reynolds number in the range $Re_l = 1$–1000; this was done for two different configurations of streamwise gap between the fins ($s_x = 0.5R, 2R$) and one selected value of the capillary number ($Ca_l = 0.04$).

### 5.1. Bubble and liquid film dynamics for reference case

This section presents the results for the reference case run with $Ca_l = 0.04$, $Re_l = 1$, $s_x = 0.5R$, and $L_b = 12R$. Fig. 4(a) displays a snapshot of bubble profile, velocity and pressure contours, extracted on a horizontal centreplane ($z = 0$), when the bubble flows in the terminal steady-periodic regime. It can be seen that the cylinders modify the shape of the bubble that indents under the effects of the cylinders, while it extends towards the liquid in the gap between the cylinders. The velocity is higher inside the bubble because the gas flows downstream at a higher speed than the liquid, and localised velocity maxima are visible in the centreline between cylinders. The pressure decreases in the liquid in the streamwise direction due to the friction and pressure drag generated by the cylinders. The pressure in the bubble is larger than that in the liquid regions next to convex interface profiles, e.g. near bubble nose, rear, and in the gap between the cylinders. However, in the correspondence of concave interface regions, such as in the liquid films formed between the bubble and the cylinders, the interface curvature becomes negative (see also Fig. 2(a) and (c)) and thus the pressure in the film is larger than that in the bubble and the surrounding liquid regions, as revealed by Fig. 4(b) where the contours of the pressure field in the film region around cylinder 13 are depicted. This generates circumferential draining flows

that drive liquid out of the thin film region as the bubble translates downstream, as demonstrated by the velocity vectors in Fig. 4(b), and contribute to the monotonic thinning of the liquid film as time elapses.

The liquid film and bubble dynamics as the bubble travels through the domain are explained by means of Fig. 4(c) and (d). Fig. 4(d) plots the velocity of the bubble front, centre of mass and rear, evaluated respectively as $U_{b,N} = dx_N/dt$, $U_{b,c-m} = dx_{c-m}/dt$ and $U_{b,R} = dx_R/dt$, with x_N, x_{c-m}, and x_R being the streamwise coordinates of bubble nose tip, centre of mass, and rear tip; the velocity values are reported as a function of the bubble nose position. The bubble does never achieve a steady terminal velocity, but the velocity experiences oscillations due to the influence of the cylinders. Every time the bubble nose or rear pass through a new set of pins, the bubble experiences a restriction on the cross-section, leading to an increase in velocity; by contrast, when the bubble leaves the set of pins, the cross-section increases, which results in a reduction of the bubble velocity. The bubble nose quickly reaches a steady-periodic dynamics as $x_N/R > 20$, identified by velocity oscillations exhibiting a constant average value. The bubble rear achieves a steady-periodic regime slightly later, when the bubble nose is past the coordinate $x_N/R \approx 25$. At this instant, the tip of the bubble rear is located at about $x_R/R \approx 15$ (the bubble is about $10R$ long under these conditions), which corresponds to cylinder number 6 under the present setup. Therefore, the whole bubble achieves a steady-periodic regime after the rear has passed cylinder 6; this is verified by the film thickness plots in Fig. 4(c).

Fig. 4(c) reports the dimensionless liquid film thickness, measured on the horizontal centreplane $z = 0$ along the y direction in the point where the distance between the cylinders is the smallest, which corresponds to $\theta = 0$ in Fig. 2(d). The film thickness is reported as a function of the bubble nose streamwise distance from the cylinder centre, $x_N - x_c$, and it is measured over five consecutive cylinders (cylinders 8th-12th) to verify that the thin film dynamics has reached a steady regime. This is verified by the fact that all film thickness curves overlap. The liquid film thickness decreases quickly during the initial stages of thin film formation around the cylinder, $(x_N - x_c)/R < 2$. After this initial
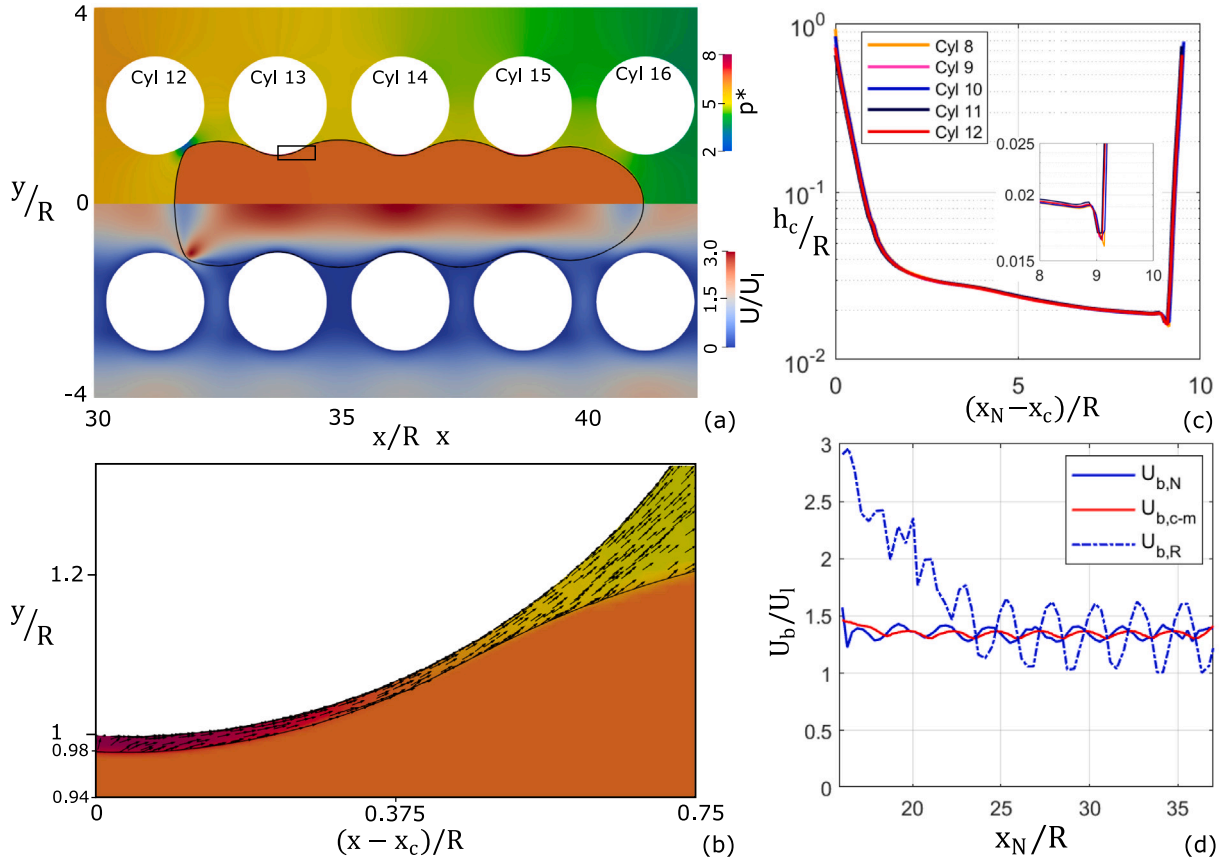
Fig. 4. Results for reference case run with $Ca_l = 0.04$, $Re_l = 1$, $s_x = 0.5R$, and $L_b = 12R$. (a) Sketch of bubble profile, velocity (bottom half) and pressure (top half) on a horizontal centreplane ($z = 0$), extracted at nondimensional time $t^* = tU_l/R = 18.8$. The velocity field is rescaled by the average liquid speed in the channel formed between the arrays of pin-fins (U_l); the pressure field is rescaled by the capillary pressure $p_{ref} = \sigma/R$; the black solid line identifies the bubble profiles. Flow is from left to right. (b) Close-up view of the pressure field and velocity vectors in the thin film region around cylinder 13, indicated with the black rectangle in (a). (c) Evolution of the dimensionless liquid film thickness h_c/R during the transit of the bubble, measured over 8th to 12th cylinders, and reported as a function of the bubble nose streamwise distance from the cylinders centres, $x_N - x_c$. The inset shows a close-up view of the data near the bubble rear. (d) Evolution of the bubble nose ($U_{b,N}$), centre of mass ($U_{b,c-m}$) and rear ($U_{b,R}$) velocity while the bubble flows downstream the channel.

film has formed, its thickness continues decreasing monotonically as the bubble nose travels further downstream the channel, although at a slower rate than that detected during the initial stages. The monotonic thinning of the film when $(x_N - x_c)/R > 2$ can be ascribed to draining flows driven by capillarity both in the circumferential direction, as explained in the paragraph above, and in the cross-stream z–direction owing to the gas–liquid interface curvature gradients established in the $y - z$ plane, see Fig. 2(c), where the latter has been observed already in square and rectangular channels (Wong et al., 1995; Hazel and Heil, 2002; Magnini and Matar, 2020b). However, this thinning trend subsides as $(x_N - x_c)/R \gg 2$ because the drainage flow rate scales with h^3 and thus quickly drops as the area available for the liquid to escape the thin film reduces. An undulation of the liquid film profile can be observed in the proximity of the bubble rear meniscus in the inset of Fig. 4(c), where the film thickness exhibits a global minimum, similarly to what observed in straight channels (Magnini et al., 2017b).

We now look at the details of the pressure field along the flow domain. Fig. 5 shows pressure profiles along four lines aligned with the x-axis: line A is aligned with the centre of the channel not occupied by the bubble (coordinates $y = 4R$, $z = 0$), while line B is located in the same channel but tangent to the cylinder surface ($y = 3R$, $z = 0$); line C ($y = R$, $z = 0$) is the corresponding line tangent to the cylinder surface but in the channel occupied by the bubble, whereas line D is the centreline of the channel occupied by the bubble ($y = 0$, $z = 0$). The pressure profiles are extracted at a selected time instant within the steady-periodic regime. Pressure decreases uniformly within

the channel not occupied by the bubble as suggested by the values extracted along lines A and B and reported in Fig. 5(b), with some undulations related to the periodic fluid acceleration and deceleration across the pin-fin matrix. The pressure at the centre of the channel occupied by the bubble (line D) follows an analogous trend, although it exhibits a sharp increase in the correspondence of the rear meniscus of the bubble, followed by a constant value when measured within the bubble, and finally by a sharp drop when crossing the front meniscus. These sudden pressure changes are due to the capillary jump in pressure across the liquid–gas interface and the pressure jump is larger at the bubble front than the rear, because the curvature of the front meniscus is larger than that at the rear as observed already in straight channels by Kreutzer et al. (2005b). The pressure extracted along line C shows regular peaks in the region occupied by the bubble, which occur where line C enters the zones occupied by the thin film. Here, the pressure is larger than that inside the bubble owing to the negative interface curvature. It is interesting to note than, on the capillary pressure scale used in Fig. 5(b), $p^* = p/(\sigma/R)$, the max pressure difference between $p_C - p_D$ evaluated over every peak of p_C is on the order of 1, because the main contribution to the interface curvature in these points comes from that established on the $x-y$ plane, which is of magnitude $\kappa_{xy} \approx 1/R$ as the interface profile follows closely the cylinder surface.
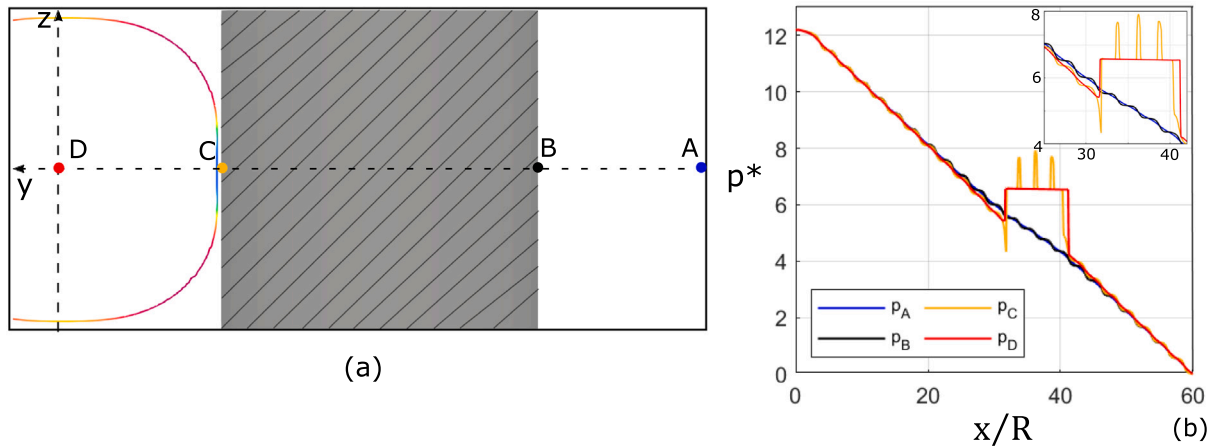
Fig. 5. Results for reference case run with $Ca_l = 0.04$, $Re_l = 1$, $s_x = 0.5R$, and $L_b = 12R$. (a) Illustration of pressure measurement points on the domain cross-section. The liquid–gas interface profile is also shown, extracted on the same section of the domain as indicated in Fig. 2(b). (b) Streamwise evolution of the pressure field along the axial lines passing through the four points indicated in (a), extracted at time $t^* = 18.8$, when the bubble flows in the steady-periodic regime.

5.2. Effect of the capillary number

This section presents a systematic analysis of the effect of the capillary number on the bubble and liquid film dynamics in the visco-capillary regime. The capillary number is varied in the range $Ca_l = 0.04–1$, while the Reynolds number is set to a small value, $Re_l = 1$, for which inertial effects are expected to be negligible (Kreutzer et al., 2005b). Fig. 6 illustrates different features of the liquid–gas interface extracted in the correspondence of cylinder 12, when the bubble nose is $9R$ downstream the cylinder centre, e.g. $(x_N - x_c)/R = 9$ in Fig. 4(c). Fig. 6(a) shows the bubble cross-sectional profiles taken at $x = x_c$, with x_c being the coordinate of the cylinder centre, for different capillary numbers. The cross-sectional interface profile is nearly axisymmetric for $Ca_l \geq 0.1$, whereas for smaller capillary numbers the profile flattens near the top wall and the cylinder surface. Along the cylinder surface, $y/R = 1$ in Fig. 6(a), a very thin film forms and as the capillary number is reduced this film extends further on the vertical (z) direction, forming a dimple similarly to what observed in square channels (Magnini and Matar, 2020a). However, in square channels the critical capillary number at which the dimple is formed is about $Ca_l = 0.01$, which is one order of magnitude smaller than the pin fin case. Fig. 6(b) presents the dimensionless liquid film thickness around a cylinder as a function of a local circumferential coordinate θ, for different capillary numbers, measured on the horizontal centreline plane ($z = 0$). As the capillary number is reduced starting from the highest value tested, $Ca_l = 1$, the liquid–gas interface approaches the cylinder surface and the shortest distance between interface and solid wall is detected at $\theta = 0$, i.e. in the correspondence of a line connecting the cylinders centres along the width-wise direction, where we identify $\theta = 0$. When the liquid capillary number decreases below 0.1, a thin liquid film forms around the cylinder surface in the circumferential direction. As the capillary number is reduced further, the liquid film thins at a slower rate but it tends to cover a wider portion of the cylinder wall. The curvature of the liquid film, observed from a $(r = R, \theta, z = 0)$ line on the cylinder wall, changes sign and two dimples are formed identifying a minimum film thickness value at symmetric circumferential positions with respect to $\theta = 0$. The dimples move sideways as the capillary number decreases and at the lowest capillary number tested, $Ca_l = 0.04$, these are located at about $\theta = \pm30$ degrees. A similar liquid film dynamics over a curved surface was observed by Moran et al. (2021) on the top surface of long bubbles travelling in horizontal channels under Bond numbers slightly above unity, where an asymmetrical thinning of the liquid film was observed as effect of draining downward flows triggered by gravity. All the data for centre (h_c) and minimum film thickness values (h_{min}) extracted on the $z = 0$ centreplane for cylinder number 12 at

different capillary numbers are compiled in Fig. 6(c,d). As a reference, the graphs include also the film thickness predictions obtained using Aussillous and Quéré (2000) correlation for circular channels and the results of the numerical simulations of Magnini and Matar (2020a) for square channels. Furthermore, the graphs report also the results of the simulations of a preliminary study that we conducted in the same conditions, but using a two-dimensional geometry which disregarded the z direction. Both the centre and minimum film thicknesses decrease quickly as the capillary number is decreased until the critical capillary number $Ca_l = 0.1$ is reached, and a thin film begins coating the cylinder surface. Below this critical value, the reduction of h subsides similarly to what is observed in square channels but below $Ca_l = 0.01$. In general, the film thickness around the cylinders is always significantly smaller than that achieved in circular and square channels, in the range of capillary numbers investigated; however, extrapolation of the trends in the figures suggest that when $Ca_l < 0.04$ liquid films in square channels may be smaller than those around pin fins. It is interesting to note that the two-dimensional simulations yield values of the film thickness that agree well with the three-dimensional simulations at larger capillary numbers, $Ca_l \geq 0.2$, where surface tension is less important, whereas the agreement worsens at lower capillary numbers. This is expected, as two-dimensional simulations cannot account for the interface curvature on the $y - z$ cross-sectional plane and thus are missing the associated contribution to the capillary force. Further insight into the dynamics of the whole bubble when varying capillary numbers is provided with Fig. 7. As the capillary number increases and viscous forces become more important, the bubbles elongate in the flow direction and expand less in the gap between the cylinders. The shape of the bubble rear, emphasised with the close-up view in Fig. 7(b), is rounded as long as surface tension forces remain important, $Ca_l \leq 0.1$, whereas it flattens for large capillary numbers as previously observed for circular tubes (Magnini et al., 2017a) and eventually exhibits time-dependent patterns and fragmentation when $Ca_l = 1$; note that, as $Re_l = 1$, the Weber number of the flow becomes of the order of unity for $Ca_l = 1$, and therefore inertial effects triggering time-dependent patterns at the bubble tail may become relevant in these conditions (Sharaborin et al., 2021). Fig. 7(c) shows the values of the bubble-to-liquid velocity ratio when varying the capillary number. The bubble speed is always larger than the average liquid speed in the channel formed between the pin fin arrays, so that $U_b/U_l > 1$ for the entire range of conditions studied. The bubble speed is very close to the values reported for square channels in previous studies (Magnini and Matar, 2020a; de Lózar et al., 2008), although bubbles travelling through pin fin arrays are slightly faster, in particular in the higher range of the Ca_l tested. This can be explained by the fact that as the bubble nose progresses between two consecutive pin fins, the liquid can be displaced sideways across the gap between the cylinders, thus offering less resistance to the bubble advancement.
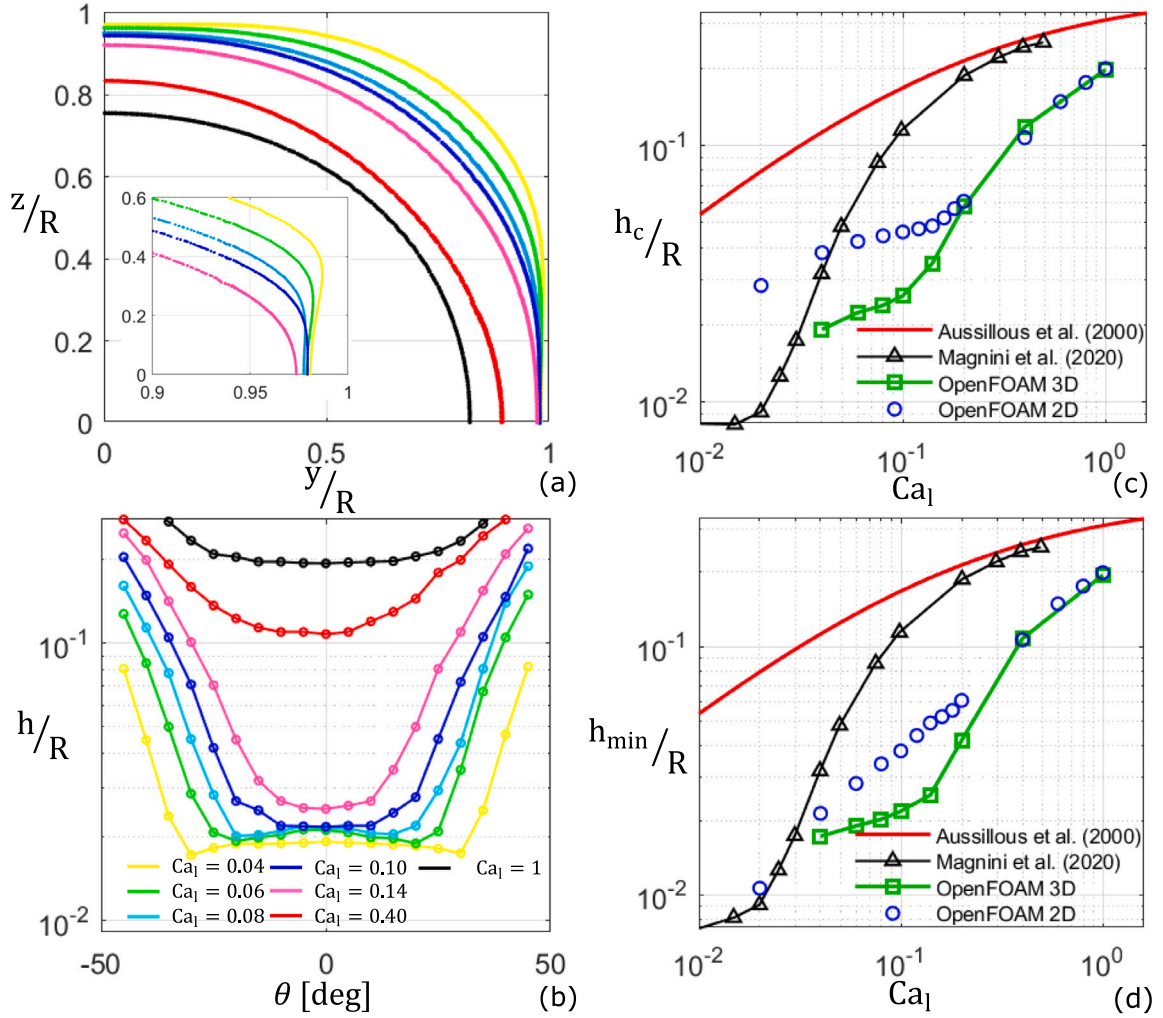
Fig. 6. Systematic analysis of the capillary number effect, for $Ca_l = 0.04$–1, on the bubble and liquid film shape; other conditions are $Re_l = 1$, $s_x = 0.5R$, and $L_b = 12R$. All interface profiles and film thickness in this figure are measured around cylinder 12, where the bubble dynamics has reached steady-state. All data are extracted at a time instant when the bubble nose is $9R$ downstream cylinder 12. (a) Cross-sectional (y–z plane) liquid–gas interface profiles for different capillary numbers measured in correspondence of the centre of the cylinder; the inset gives a close-up view near the cylinder wall, where $y/R = 1$. (b) Dimensionless local liquid film thickness (h/R) measured on the centreplane ($z = 0$) around the cylinder; see Fig. 2(d) for the notation. The legend in (b) applies also to (a). (c–d) Dimensionless liquid film thickness measured on the plane $z = 0$ (c) at the cylinder centre (h_c/R) and (d) minimum film thickness (h_{min}/R), versus liquid capillary number (Ca_l). As a reference, the graphs in (c) and (d) include also the liquid film thickness prediction for a circular channel obtained using Aussillous and Quéré (2000) correlation, the film thickness data for square channels reported by Magnini and Matar (2020a), and the data for flow past pin fins obtained with preliminary two-dimensional simulations.

5.3. Effect of the streamwise distance between pin fins

This section investigates the influence of the streamwise gap between the pins on the dynamics of the flow. The results of simulations performed varying the pitch in the range $s_x = 0.125R$–$2R$ are reported, for three selected values of the capillary number, $Ca_l = 0.04, 0.1$ and 0.2, while $Re_l = 1$, and $L_b = 12R$. The different gaps between the pins can also be converted into porosity values for the geometry. The porosity can be estimated as $\phi = 1 - \pi R^2/(d_x d_y)$, with d_y being constant ($d_y = 4R$) and $d_x = s_x + 2R$. The range of porosity obtained for $s_x = 0.125R$–$2R$ is $\phi = 0.63$–0.8, with the reference case $s_x = 0.5R$ corresponding to a porosity of 0.69.

For all the other studies previously shown, a reference configuration $s_x = 0.5R$ was adopted, which is a typical setup in micro-pin fin heat exchangers (Kosar and Peles, 2006; Isaacs et al., 2012). In Fig. 8(a-f), snapshots of bubble profiles, velocity and pressure contours for cases with different geometry are reported. It can be observed that the cylinders setup modifies strongly the shape of the bubble. The increase of the pitch between the fins favours the bubble to expand between the gaps, as a consequence the bubble is shorter. We observed that $s_x = 2R$

was a limit configuration in the present setup. For $s_x > 2R$, the bubble expanded excessively in the cross-stream direction and eventually remained trapped in the region bounded between four adjacent pin fins, with the incoming liquid bypassing it through the neighbour channels. As s_x is reduced, the bubble exhibits smaller bulges and indentations, taking a more slender profile between the pin fin arrays similarly to what would be expected in a straight wall configuration. Therefore, we can consider the straight wall configuration as an asymptotic case where $s_x \rightarrow 0$.

Liquid film thickness and bubble speed trends for different values of s_x and Ca_l are summarised in Fig. 8(g) and (h). Overall, we can observe that the distance between the cylinders has a significant influence on the film thickness established between the bubble and the cylinders walls. There is a systematic trend of h_c/R to increase as $s_x/R > 0.5$, which can be ascribed to a larger portion of the cylinders surface becoming covered by the liquid film. The leading and trailing edge of the meniscus formed around the cylinders get farther from the $\theta = 0$ location where h_c is measured, as s_x is increased above 0.5. This causes a slight increase in h_c, similarly to what is observed in square channels as the capillary number is reduced and a dimple forms over the channel
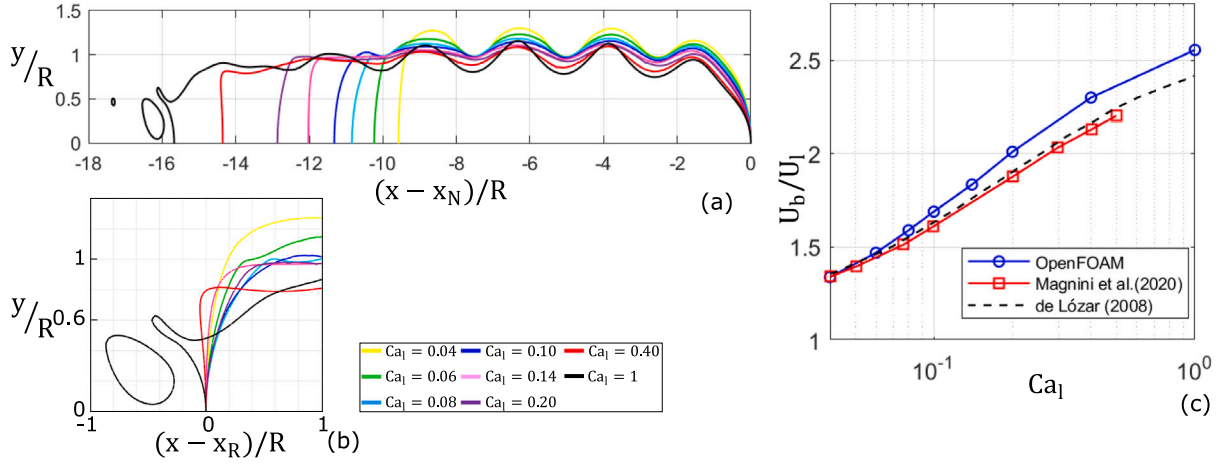
Fig. 7. Systematic analysis of the capillary number effect, for $Ca_l = 0.04–1$, on the bubble shape and speed; other conditions are $Re_l = 1$, $s_x = 0.5R$, and $L_b = 12R$. (a) Liquid–gas interface profiles on the centreplane $z = 0$ extracted at steady-state, for different capillary numbers. All profiles are extracted at the instant where the bubble nose (x_N) is about $9R$ downstream the centre of cylinder number 12. The profiles in (a) are shifted to have same x_N. (b) Close-up view of the profiles in (a) near the bubbles rear, now shifted to have the same position of the bubble rear x_R. (c) Dimensionless velocity of the bubble nose against liquid capillary number (Ca_l). As a reference, the graph contains the results of the numerical simulations of Magnini and Matar (2020a) and de Lózar et al. (2008) for square channels.
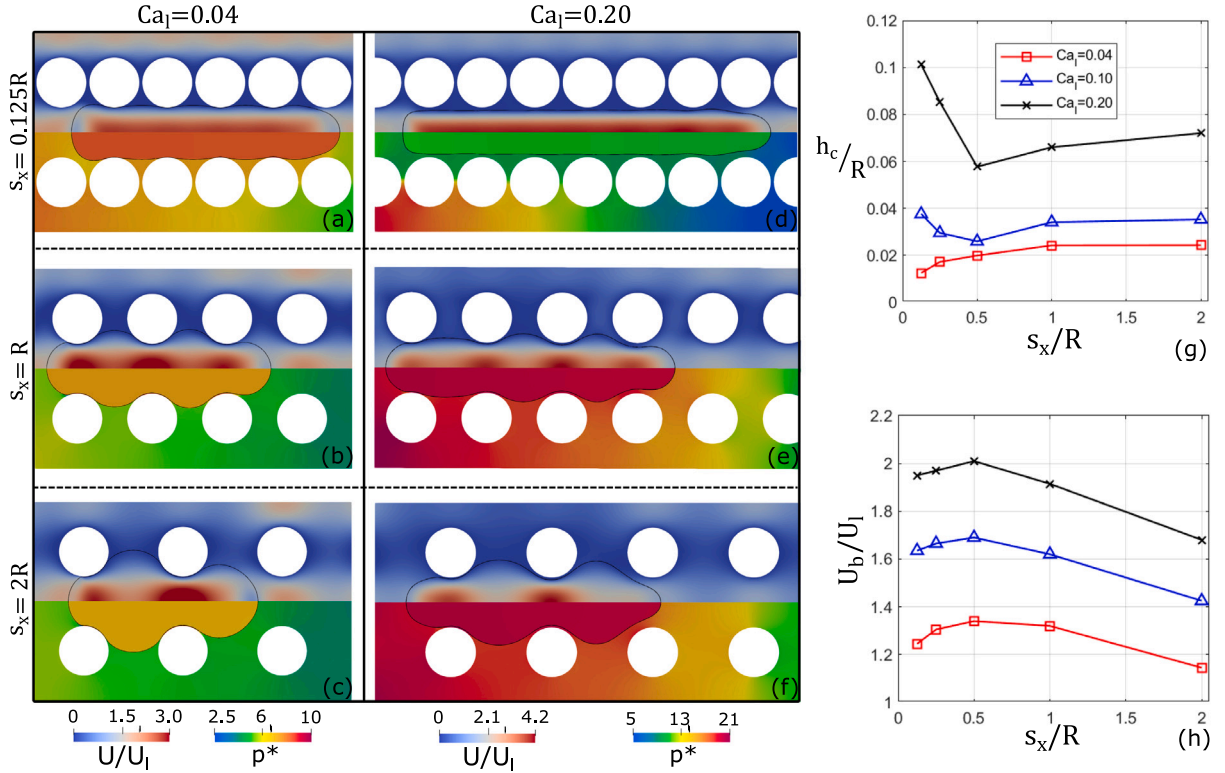
Fig. 8. Systematic analysis of the effect of the streamwise distance between the pin fins, for $s_x = 0.125R - 2R$; other conditions are $Ca_l = 0.04, 0.1, 0.2$, $Re_l = 1$ and $L_b = 12R$. (a–f) Snapshots of bubble profiles (black lines), velocity (top half) and pressure contours (bottom half) for different values of s_x. (g) Dimensionless liquid film thickness (h_c/R) and (h) bubble velocity against streamwise gap between the pins (s_x) for different capillary numbers (Ca_l). The legend in (g) applies also to (h).

walls (Magnini and Matar, 2020a). The bubble speed decreases as s_x increases in the same range, because the bubble tends to expand in the cross-stream direction as the channelling effect of the cylinders on the flow is reduced. As $s_x \to 0$, we would expect h_c to converge towards the value for a square channel, which is larger than the thicknesses observed for $s_x = 0.5$ over the entire range of Ca_l studied in this work, see Fig. 6(c). This is in agreement with the increasing trend of h_c/R as s_x is reduced below 0.5 in Fig. 8(g) for $Ca_l = 0.1$ and 0.2, which identifies a minimum film thickness value at $s_x = 0.5R$ for both capillary numbers. However, this trend is not observed for the smallest

capillary number tested, $Ca_l = 0.04$, where h_c decreases monotonically in the range of s_x investigated. It is plausible that the expected increase of h_c towards the square channel values is shifted towards lower values of s_x than those investigated in this work at small Ca_l, where surface tension becomes dominant and the liquid–gas interface is to a larger extent impacted by the topography of the domain walls.

In summary, the liquid film thickness is very sensitive to the streamwise pitch of the pin fins, and for a constant value of the liquid flow rate (or liquid capillary number) h_c may change by a factor of 2 when s_x is varied in the range $s_x = 0.125R–2R$.
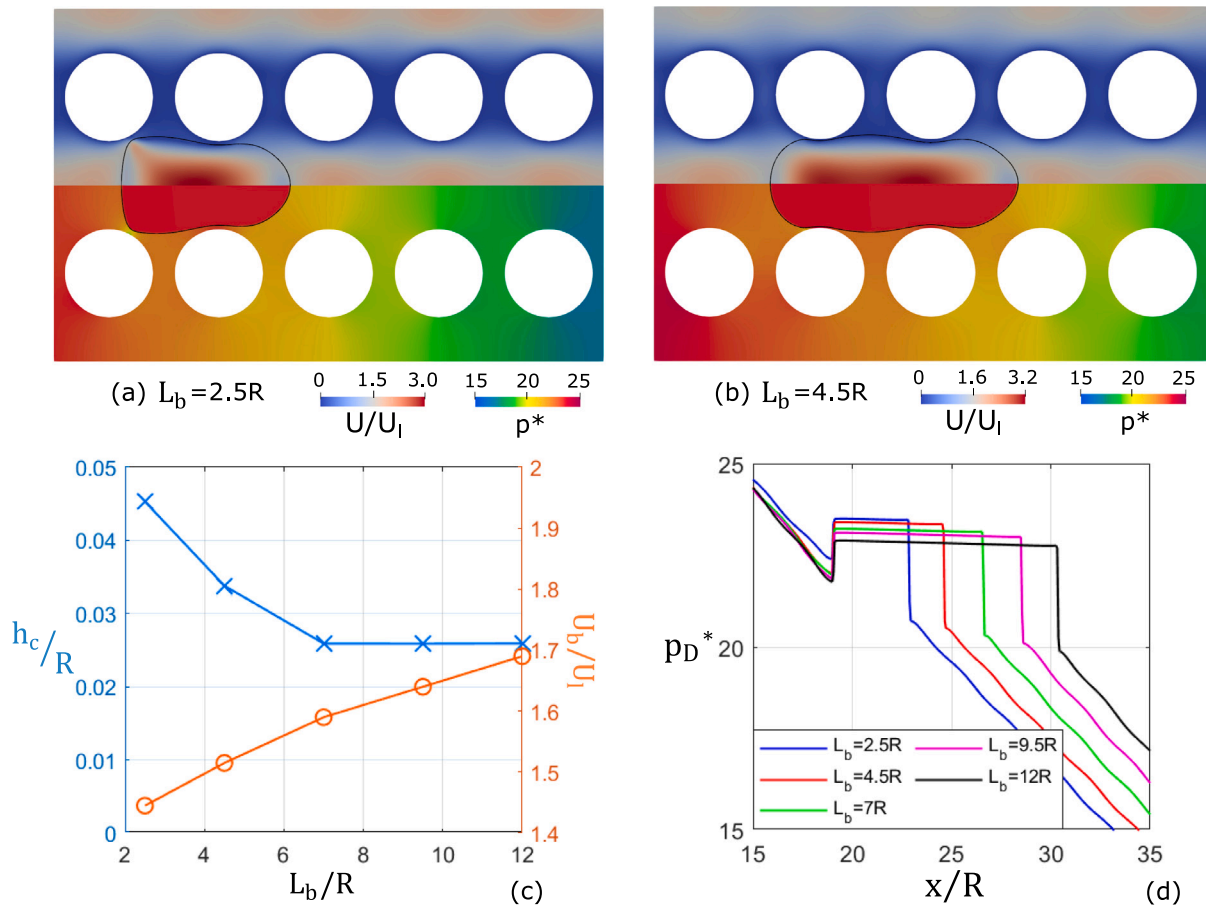
Fig. 9. Systematic analysis of the effect of the initial bubble length, for $L_b/R = 2.5 - 12$; other conditions are $Ca_l = 0.1$, $Re_l = 1$ and $s_x = 0.5R$. (a–b) Snapshots of bubble profiles (black lines), velocity (top half) and pressure (bottom half) contours, for (a) $L_b = 2.5R$ and (b) $L_b = 4.5R$. (c) Liquid film thickness and bubble velocity against initial bubble length (L_b). (d) Streamwise pressure profiles extracted along the centreline of the channel, as indicated in Fig. 5(a), when the bubble flows in the steady-periodic regime.

5.4. Effect of the bubble length

Multiphase flow within microchannels presents different flow regimes depending on the volume of gas being mobilised and on the relative velocity between the liquid and gas phases (Triplett et al., 1999). In the case of bubbles, flow regimes can be separated into bubbly flows, when the equivalent diameter of a bubble is smaller than the channel size, and elongated bubbles when bubbles are larger. Within straight channels, it has been verified in numerous studies that when the bubble length is more than twice the channel diameter, the bubble length has no impact on the speed of the bubble (Khodaparast et al., 2015). Within circular channels, the bubble length has no effect on the liquid film thickness provided that $L_b/R > 4$ (Khodaparast et al., 2015), although the bubble length necessary to achieve a flat film increase with capillary and Reynolds numbers (Magnini et al., 2017b). In noncircular channels, the bubble length may have an impact on the liquid film thickness due to the capillary-induced drainage flows in the liquid film, depending on capillary number and channel aspect-ratio (Magnini et al., 2022). Therefore, this section presents the results of an analysis of the bubble length. The initial bubble length is varied within the $L_b = 2.5R–12R$, while fixing $Ca_l = 0.1$, $Re_l = 1$ and $s_x = 0.5R$.

Fig. 9(a,b) provide snapshots of the bubble dynamics during the steady-periodic regime, for relatively short bubbles. Although no significant differences emerge between the two figures, the liquid film deposited around the cylinder for the shortest bubble, $L_b = 2.5R$ in Fig. 9(a), is evidently thicker than that established for $L_b = 4.5R$ in Fig. 9(b). Note that for $L_b = 2.5R$ the bubble length is similar to the streamwise distance between the centres of two consecutive pins, and therefore only one or two cylinders maximum are simultaneously

engaged by the bubble during its flow, making the dynamics of the rear meniscus more dependent on that of the front meniscus.

This qualitative information is supported by the liquid film thickness data presented in Fig. 9(c). In this section, the liquid film thickness is still measured around cylinder number 12, but now it is measured at the time instant when the bubble nose is only $2.5R$ downstream the cylinder centre, so that the same measurement point is available for all bubble lengths. In the previous sections, where $L_b = 12R$, the measurement point was at a distance of $9R$ behind the bubble nose, but this was not possible when testing shorter bubbles. When bubbles are shorter than $7R$, the liquid film thickness seems to increase monotonically when reducing the bubble length. This can be ascribed to the fact that there is no sufficient time for the liquid in the film to drain, thus leaving a thicker liquid layer over the cylinder surface. When $L_b/R > 7$, a threshold slightly larger than that reported for circular channels, the bubble length does no longer impact the liquid film thickness for the capillary number studied. Note that the difference in liquid film thickness between the two limiting cases $L_b/R = 2.5$ and $L_b/R = 12$ is significant, as it amounts to a factor of 2. The bubble speed increases monotonically with the bubble length, although the difference in bubble speed between $L_b/R = 9.5$ and 12 is only about 5%. Last, Fig. 9(d) shows the pressure profiles along the channel centreline for the different cases. Shorter bubbles exhibit shorter regions where the pressure increases due to the capillary contribution, but no other differences are apparent among the different configurations.

5.5. Effect of the Reynolds number

Inertial forces are typically regarded as secondary effects in microfluidics, however, there exist engineering applications where flows
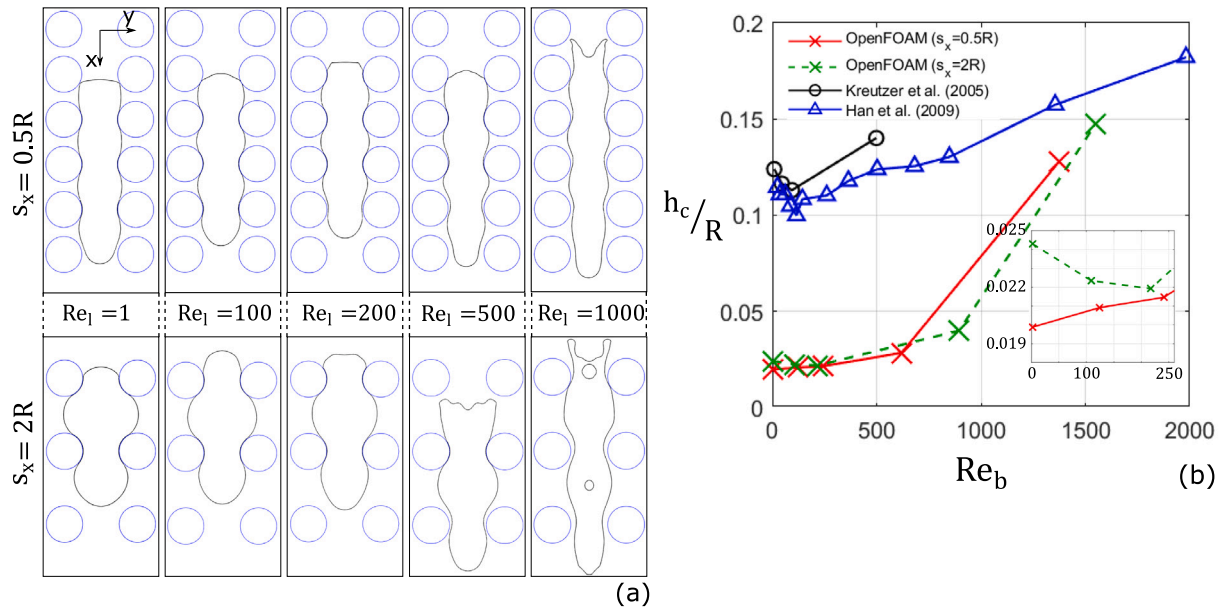
Fig. 10. Systematic analysis of the effect of the Reynolds number, for $Re_l = 1 - 1000$, in two different geometrical configurations $s_x = 0.5R, 2R$; other conditions are $Ca_l = 0.04$ and $L_b = 12R$. (a) Snapshots of bubble profiles for different Reynolds numbers and different streamwise gap between the pins. (b) Dimensionless liquid film thickness (h_c/R) against Reynolds number of the bubble $(Re_b = 2\rho_l U_b R/\mu_l)$; the inset shows a close-up view of the data at small Reynolds numbers. As a reference, the plot also includes the liquid film thickness results of Kreutzer et al. (2005b) and Han and Shikazono (2009a) for $Ca_l = 0.04$ in circular pipes.

in sub-millimetric channels can still achieve Reynolds numbers as high as 10^3 (Kosar et al., 2005; Zhao et al., 2016). This happens in particular in heat transfer elements, where high flow rates are utilised to achieve high convective heat transfer. In two-phase flow, there is general consensus that inertia has a considerable impact on the bubble dynamics and shape when $Re > 100$ (Kreutzer et al., 2005b; Han and Shikazono, 2009a), and generally inertial forces impact the bubble dynamics by thinning the liquid film thickness for Reynolds numbers in an intermediate range of $Re = 100$–500, and thickening it at higher Reynolds numbers.

In this section, we present the results of simulations run by systematically varying the Reynolds number in the range $Re_l = 1$–1000, which resulted into a range of bubble Reynolds numbers $Re_b = 1$–1600. The capillary number is fixed to a value of $Ca_l = 0.04$, and two different values of streamwise distance between the pin fins were taken into account $s_x = 0.5R, 2R$, with a constant initial bubble length of $L_b = 12R$.

Since cross-flow past arrays of cylinders may exhibit time-dependent patterns known as von Kármán vortex streets, all simulations were first run in single-phase for a long time (up to $t^* = tU_l/R = 150$) to verify whether vortex shedding appeared in the conditions investigated, for both $s_x = 0.5R$ and $2R$. No time-dependent patterns were observed in the entire range of Reynolds numbers tested. Zhang et al. (2019) performed experiments of flow past one confined cylinder in a microfluidic channel and observed that the critical Reynolds number at which vortex shedding appeared, evaluated as $Re = \rho U_m D/\mu$ with U_m being the maximum velocity upstream of the cylinder and D the cylinder diameter, increased from 200 to 550 when decreasing the channel height-to-diameter ratio from 3 to 1, while maintaining the same width-to-diameter ratio of 3. In our case, the height-to-diameter ratio of the channel is 1 and the width-to-diameter can be considered as 1. Furthermore, the maximum liquid speed upstream the cylinders bank is about half that used to calculate the Reynolds number in this work, and therefore the range of Reynolds numbers considered in our study and the level of confinement are well within the range where Zhang et al. (2019) observed no vortex shedding. We attempted tests for larger gaps between the cylinders, $s_x = 3R$, and in this case we observed the appearance of time-dependent vortices at Reynolds numbers of about

500, but these conditions were not eventually studied in two-phase regime.

Fig. 10(a) shows snapshots of the bubble dynamics for all values of s_x and Re_l investigated. For values of Re_l up to about 500, the bubble retains the capillary-driven shape with rounded nose and tail, although the nose becomes more slender as already reported by Edvinsson and Irandoust (1996). When $Re_l = 1000$, bubbles are considerably longer and the interface exhibits time-dependent patterns that cause fragmentation of the rear meniscus and entrainment of liquid within the gas. Liquid films are apparently thicker, and the profile of the film around the cylinders in the circumferential direction is strongly asymmetric, with thinner films on the downstream quarter of the cylinder surface ($\theta > 0$ in Fig. 2(d)) and thicker films on the upstream quarter ($\theta < 0$).

The film thickness data versus Re_l are compiled in Fig. 10(b), where experimental data from the literature for circular channels are also included as a reference. In the low-Reynolds number range, the film thickness is little sensitive to Re_l and the values for flow past pin fins are much smaller than those in tubes, as already discussed previously. However, at the largest Reynolds number tested, $Re_l = 1000$, h_c/R increases by a factor of 5 from the value achieved in the visco-capillary regime, also approaching the values measured in tubes. As observed in Fig. 10(a), there is a distinct change in bubble dynamics from $Re_l = 500$ to $Re_l = 1000$, where inertial forces have a strong impact on the bubble shape and film topology. Therefore, the presence of the cylinders seems to amplify the effect of inertia as compared to two-phase flow in straight channels, and the impact of the Reynolds number on the bubble dynamics, film morphology and film thickness becomes of primary importance.

6. Conclusions

The shape and dynamics of long gas bubbles propagating through circular pin fin arrays have been examined in detail for a range of liquid capillary numbers $Ca_l = 0.04$–1, streamwise pitch of the cylinders $s_x = 0.125R$–$2R$, bubble length $L_b = 2.5R$–$12R$ and Reynolds numbers $Re_l = 1$–1000, thus covering both the visco-capillary and visco-inertial regimes, conditions that may be relevant both for flow in porous media and micro-pin fin heat exchangers. The study is based on the

results of three-dimensional numerical simulations conducted adopting a geometric VOF method as implemented in the TwoPhaseFlow library for OpenFOAM released by Scheufler and Roenby (2021). The computational mesh is always sufficiently fine to fully capture the thin liquid film trapped between the bubble and the obstacles, thus allowing to quantify its thickness and morphology at all conditions investigated. The main conclusions of this study are as follows:

- The bubble nose and rear menisci experience periodic accelerations and decelerations as the bubble propagates through the arrays, but eventually achieve a steady-periodic flow regime where their time-averaged values are the same.
- As the bubble propagates through the arrays of pin fins, it wraps around their surface leaving a thin liquid film in between. This film exhibits some of the features characteristic of film deposition in straight channels; it thins monotonically towards the bubble rear, and its thickness varies as a function of the capillary number. Under the conditions investigated, the film thickness is always smaller than those reported for circular and square channels.
- When $Ca_l < 0.1$, interfacial dimples form over the flat channel walls and the pin fins surfaces, causing localised peaks of capillary pressure that induce strong drainage flows that push liquid out of the film.
- Bubble and film dynamics are very sensitive to the streamwise distance between the cylinders s_x. As $s_x \to 0$, the configuration converges to that of a straight channel and the liquid film thickness increases. As s_x increases, the bubble is less guided in the downstream direction and tends to expand in the gap between the cylinders, giving way to thicker liquid films. In between these two limiting situations, a minimum film thickness condition is identified.
- Bubbles shorter than $L_b/R = 7$ exhibit increasing values of the film thickness as their length is decreased, but for $L_b/R > 7$ the bubble length has a negligible impact on its dynamics.
- Inertial effects are mild when $Re_l \le 500$ but, for larger Reynolds numbers, the bubble shape exhibits strong time-dependent patterns leading to fragmentation of its rear meniscus and to liquid films that are more than 5 times thicker than those observed in the visco-capillary regime.

This work emphasises that the morphology and thickness of liquid films deposited by long bubbles flowing in non-straight and complex confined geometries are profoundly different from those reported for circular and noncircular straight channels. As such, models and correlations specific for the geometrical configuration of interest should be used to predict relevant liquid–gas interface features.

CRediT authorship contribution statement

I. El Mellas: Conceptualization, Methodology, Software, Validation, Formal analysis, Investigation, Visualization, Data curation, Writing – original draft, Writing – review & editing. **F. Municchi:** Methodology, Software, Supervision, Writing – review & editing. **M. Icardi:** Conceptualization, Methodology, Supervision, Writing – review & editing. **M. Magnini:** Conceptualization, Methodology, Supervision, Data curation, Project administration, Resources, Writing – review & editing, Funding acquisition.

Declaration of competing interest

The authors declare that they have no known competing financial interests or personal relationships that could have appeared to influence the work reported in this paper.

Data availability

The data that has been used is confidential.

Appendix. Simulation parameters in dimensional units

OpenFOAM solves the fluid flow equations in dimensional form and thus requires input parameters in dimensional units. All our simulation cases are parameterised using hard-coded values of $R = 1$ m for the pin fin radius, $\rho_l = 1$ kg/m³ for the liquid density, and $U_l = 2$ m/s as the average velocity of the liquid between the pin fin arrays; since the pin fin arrays occupy half of the domain cross-section, the velocity boundary condition set at the domain inlet is 1 m/s. The bubble density is set to $\rho_b = 0.001$ kg/m³ to achieve a liquid-to-gas density ratio of 1000. The liquid dynamic viscosity depends on the liquid Reynolds number of the simulation, $\mu_l = 2\rho_l U_l R/Re_l$. The surface tension coefficient is calculated from the liquid capillary number, $\sigma = \mu_l U_l/Ca_l$. For example, the case run with $Ca_l = 0.04$ and $Re_l = 1000$ was obtained by using $\mu_l = 0.004$ kg/(m s) and $\sigma = 0.2$ N/m. Last, the bubble dynamic viscosity is calculated from μ_l to achieve a liquid-to-gas dynamic viscosity ratio of 100, thus $\mu_b = 0.00004$ kg/(m s) for the case indicated above. The typical end time of the simulation in these units is of about 10 s.

References

Abadie, T., Aubin, J., Legendre, D., 2015. On the combined effects of surface tension force calculation and interface advection on spurious currents within volume of fluid and level set frameworks. J. Comput. Phys. 297, 611–636.

Anjos, G.R., 2021. Numerical investigation of two-phase flows in corrugated channel with single and multiples drops. Fluids 6, 13.

Aussillous, P., Quéré, D., 2000. Quick deposition of a fluid on the wall of a tube. Phys. Fluids 12, 2367–2371.

Balestra, G., Zhu, L., Gallaire, F., 2018. Viscous Taylor droplets in axisymmetric and planar tubes: from Bretherton's theory to empirical models. Microfluid Nanofluid 22 (10).

Brackbill, J.U., Kothe, D.B., Zemach, C., 1992. A continuum method for modeling surface tension. J. Comput. Phys. 100, 335–354.

Bretherton, F.P., 1961. The motion of long bubbles in tubes. J. Fluid Mech. 10, 166–188.

Cummins, S.J., Francois, M.M., Kothe, D.B., 2005. Estimating curvature from volume fractions. Comput. Struct. 83, 425–434.

Edvinsson, R., Irandoust, S., 1996. Finite-element analysis of Taylor flow. AIChE J. 42, 1815–1823.

Falsetti, C., Jafarpoorchekab, H., Magnini, M., Borhani, N., Thome, J.R., 2017a. Two-phase operational maps, pressure drop, and heat transfer for flow boiling of r236fa in a micro-pin fin evaporator. Int. J. Heat Mass Transfer 107, 805–819.

Falsetti, C., Magnini, M., Thome, J.R., 2017b. Flow boiling heat transfer and pressure drops of R1234ze(E) in a silicon micro-pin fin evaporator. J. Electron. Packag. 139, 031008.

Falsetti, C., Magnini, M., Thome, J.R., 2018a. Hydrodynamic and thermal analysis of a micro-pin fin evaporator for on-chip two-phase cooling of high density power micro-electronics. Appl. Therm. Eng. 130, 1425–1439.

Falsetti, C., Magnini, M., Thome, J.R., 2018b. A new flow pattern-based boiling heat transfer model for micro-pin fin evaporators. Int. J. Heat Mass Transfer 122, 1425–1439.

Ferrari, A., Lunati, I., 2013. Direct numerical simulations of interface dynamics to link capillary pressure and total surface energy. Adv. Water Resour. 57, 19–31.

Gomes Suarez, C., Noordmans, J., van der Mei, H.C., Busscher, H.J., 1999. Removal of colloidal particles from quartz collector surfaces as stimulated by the passage of liquid-air interfaces. Langmuir 15, 5123–5127.

Gupta, R., Fletcher, D.F., Haynes, B.S., 2009. On the CFD modelling of Taylor flow in microchannels. Chem. Eng. Sci. 2941–2950.

Han, Y., Shikazono, N., 2009a. Measurement of liquid film thickness in micro square channel. Int. J. Multiph. Flow 35, 896–903.

Han, Y., Shikazono, N., 2009b. Measurement of the liquid film thickness in microtube slug flow. Int. J. Heat Fluid Flow 30, 842–853.

Hazel, A.L., Heil, M., 2002. The steady propagation of a semi-infinite bubble into a tube of elliptical or rectangular cross-section. J. Fluid Mech. 470, 91–114.

Isaacs, S., Jo, K.Y., J., M.A., Yogendra, J., Zhang, Y., Bakir, S., M., 2012. Two-phase flow and heat transfer in pin-fin enhanced micro-gaps. In: 13th InterSociety Conference on Thermal and Thermomechanical Phenomena in Electronic Systems. Hong Kong, China.

Issa, R.I., 1985. Solution of the implicitly discretized fluid flow equations by operator-splitting. J. Comput. Phys. 62, 40–65.

Khodaparast, S., Magnini, M., Borhani, N., Thome, J.R., 2015. Dynamics of isolated confined air bubbles in liquid flows through circular microchannels: an experimental and numerical study. Microfluid Nanofluid 19, 209–234.

Kosar, A., Peles, Y., 2006. Convective flow of refrigerant (r-123) across a bank of micro pin fins. Int. J. Heat Mass Transfer 49, 3142–3155.

Kosar, A., Peles, Y., 2007. Boiling heat transfer in a hydrofoil-based micro pin fin heat sink. Int. J. Heat Mass Transfer 50, 1018–1034.

Kosar, A., Peles, Y., C, M., 2005. Laminar flow across a bank of low aspect ratio micro pin fins. J. Fluids Eng. 127, 419–430.

Kreutzer, M.T., Kapteijn, F., Moulijn, J.A., Heiszwolf, J.J., 2005a. Multiphase monolith reactors: chemical reaction engineering of segmented flow in microchannels. Chem. Eng. Sci. 60, 5895–5916.

Kreutzer, M.T., Kapteijn, F., Moulijn, J.A., Kleijn, C.R., Heiszwolf, J.J., 2005b. Inertial and interfacial effects on pressure drop of Taylor flow in capillaries. AIChE J. 51, 2428–2440.

Krishnamurthy, S., Peles, Y., 2010. Flow boiling heat transfer on micro pin fins entrenched in a microchannel. J. Heat Trans. 132, 041007.

Lake, L.W., 1989. Enhanced oil recovery. Prentice Hall.

van Leer, B., 1979. Towards the ultimate conservative difference scheme. v. a second-order sequel to godunov's method. J. Comput. Phys. 32, 101–136.

de Lózar, A., Hazel, A.L., Heil, M., 2007. Scaling properties of coating flows in rectangular channels. Phys. Rev. Lett. 99, 234501.

de Lózar, A., Juel, A., Hazel, A.L., 2008. The steady propagation of an air finger into a rectangular tube. J. Fluid Mech. 614, 173–195.

Magnini, M., Beisel, A., Ferrari, A., Thome, J.R., 2017a. Pore-scale analysis of the minimum liquid film thickness around elongated bubbles in confined gas-liquid flows. Adv. Water Resour. 109, 84–93.

Magnini, M., Ferrari, A., Thome, J.R., Stone, H.A., 2017b. Undulations on the surface of elongated bubbles in confined gas-liquid flows. Phys. Rev. Fluids 2, 084001.

Magnini, M., Matar, O.K., 2020a. Morphology of long gas bubbles propagating in square capillaries. Int. J. Multiph. Flow 129, 103353.

Magnini, M., Matar, O.K., 2020b. Numerical study of the impact of the channel shape on microchannel boiling heat transfer. Int. J. Heat Mass Transfer 150, 119322.

Magnini, M., Municchi, F., El Mellas, I., Icardi, M., 2022. Liquid film distribution around long gas bubbles propagating in rectangular capillaries. Int. J. Multiph. Flow 148, 103939.

Magnini, M., Thome, J.R., 2017. An updated three-zone heat transfer model for slug flow boiling in microchannels. Int. J. Multiph. Flow 91, 296–314.

Moran, H., Magnini, M., Markides, C.N., Matar, O.K., 2021. Inertial and buoyancy effects on the flow of elongated bubbles in horizontal channels. Int. J. Multiph. Flow 135, 103468.

Muradoglu, M., Stone, H.A., 2007. Motion of large bubbles in curved channels. J. Fluid Mech. 570, 455–466.

Patel, T., Patel, D., Thakkar, N., Lakdawala, A., 2019. A numerical study on bubble dynamics in sinusoidal channels. Phys. Fluids 31, 052103.

Picchi, D., Poesio, P., 2022. Dispersion of a passive scalar around a Taylor bubble. J. Fluid Mech. 951, A22.

Renfer, A., Tiwari, M.K., Tiwari, R., Alfieri, F., Brunschwiler, T., Michel, B., Poulikakos, D., 2013. Microvortex-enhanced heat transfer in 3D-integrated liquid cooling of electronic chip stacks. Int. J. Heat Mass Transfer 65, 33–43.

Roenby, J., Bredmose, H., Jasak, H., 2016. A computational method for sharp interface advection. R. Soc. Open Sci. 3, 160405.

Roland, L., Eric, T., Cesar, Z., 1988. Numerical models and experiments on immiscible displacements in porous media. J. Fluid Mech. 189, 165–187.

Safi, M.A., Prasianakis, N.I., Mantzaras, J., Lamibrac, A., Büchi, F.B., 2017. Experimental and pore-level numerical investigation of water evaporation in gas diffusion layers of polymer electrolyte fuel cells. Int. J. Heat Mass Transfer 115, 238–249.

Sauzade, M., Cubaud, T., 2018. Bubble deformations and segmented flows in corrugated microchannels at large capillary numbers. Phys. Rev. Fluids 3, 034202.

Scheufler, H., Roenby, J., 2019. Accurate and efficient surface reconstruction from volume fraction data on general meshes. J. Comput. Phys. 383, 1–23.

Scheufler, H., Roenby, J., 2021. Twophaseflow: an OpenFOAM based framework for development of two phase flow solvers. ArXiv https://arxiv.org/abs/2103.00870.

Shang, J., Flury, M., Chen, G., Zhuang, J., 2008. Impact of flow rate, water content, and capillary forces onin situ colloid mobilization during infiltration in unsaturated sediments. Water Resour. Res. 44, W06411.

Sharaborin, E.L., Rogozin, O.A., Kasimov, A.R., 2021. Computational study of the dynamics of the Taylor bubble. Fluids 6, 389.

Soulaine, C., Roman, S., Kovscek, A., Tchelepi, H.A., 2018. Pore-scale modelling of multiphase reactive flow: application to mineral dissolution with production of CO_2. J. Fluid Mech. 855, 616–645.

Taylor, G.I., 1960. Deposition of a viscous fluid on the wall of a tube. J. Fluid Mech. 10, 161–165.

Thome, J.R., Dupont, V., Jabobi, A.M., 2004. Heat transfer model for evaporation in microchannels. part i: presentation of the model. Int. J. Heat Mass Transfer 47, 3375–3385.

Thulasidas, T.C., Abraham, M.A., Cerro, R.L., 1995. Bubble-train flow in capillaries of circular and square cross-section. Chem. Eng. Sci. 50, 183–199.

Triplett, K.A., Ghiaasiaan, S.M., Abdel-Khalik, S.I., Sadowski, D.L., 1999. Gas-liquid two-phase flow in microchannels part i: two-phase flow patterns. Int. J. Multiph. Flow 25, 377–394.

Tryggvason, G., Scardovelli, R., Zaleski, S., 2011. Direct Numerical Simulations of Gas-Liquid Multiphase Flows. Cambridge University Press, Cambridge.

Wan, W., Deng, D., Huang, Q., Zeng, T., Huang, Y., 2017. Experimental study and optimization of pin fin shapes in flow boiling of micro pin fin heat sinks. Appl. Therm. Eng. 114, 436–449.

Wong, H., Radke, C.J., Morris, S., 1995. The motion of long bubbles in polygonal capillaries. part 1. thin films. J. Fluid Mech. 292, 71–94.

Zamankhan, P., Takayama, S., Grotberg, J.B., 2018. Steady displacement of long gas bubbles in channels and tubes filled by a Bingham fluid. Phys. Rev. Fluids 3, 013302.

Zhang, S., Cagney, N., Balabani, S., Naveira-Cotta, C.P., Tiwari, M.K., 2019. Probing vortex-shedding at high frequencies in flows past confined microfluidic cylinders using high-speed microscale particle image velocimetry. Phys. Fluids 31, 102001.

Zhao, H., Liu, Z., Zhang, C., Guan, N., Zhao, H., 2016. Pressure drop and friction factor of a rectangular channel with staggered mini pin fins of different shapes. Exp. Therm. Fluid Sci. 71, 57–69.